QUANTIFYING THE INFLUENCE OF TIDAL SAND WAVE ORIENTATION ON FORM ROUGHNESS

THESIS

05/07/2024

Author: Carlos Heriberto Bedon Pineda
Chair of committee: Pieter Roos
Supervisor: Laura Portos-Amill

FACULTY OF ENGINEERING TECHNOLOGY
WATER ENGINEERING AND MANAGEMENT
UNIVERSITY OF TWENTE.
MELODY

Acknowledgements

I want to thank everyone involved in carrying out this research project and all that helped me through the process.

Particularly, I want to thank my supervisors, Laura Portos-Amill and Pieter Roos, for their support, time, and feedback during the development of this thesis. Along with it, I want to thank my mom and dad, my sister, my brother, and my closest friends and relatives that energetically accompanied me emotionally through my studies.

Abstract

The Netherlands Continental Shelf, a dynamic seabed dominated by tides is characterized by the presence of sand waves. These rhythmic features have wavelengths spanning from 100 to 1000 meters, heights of several meters, and migration rates of the order of meters per year. Existing hydrodynamic models, like the Dutch Continental Shelf Model (DCSM), lack the resolution to capture these features and rely solely on calibration based on water level observations, hindering physical understanding and accurate flow representation.

While previous research explored the link between sand wave properties and form roughness under perpendicular tidal flow in a 2DV setting, this study extends the analysis to a 3D setting, adding additional complexities such as flow structures in both horizontal directions (in the presence of the Coriolis effect), the distribution of two-dimensional shear stress, and the presence of a rotated sand wave field. Our aim is to analyze the influence of sand wave field orientation relative to the dominant flow direction, as well as various sand wave characteristics (e.g., height, wavelength) on form roughness.

Using the Delft3D numerical model, we simulated tidal flow over a morphostatic bed with varying sand wave field characteristics. By considering that tidal flow is characterized by several tidal constituents, each represented by an amplitude and a phase, we establish four criteria for quantifying form roughness. The form roughness is the one that best replicates either the observed amplitude or phase of the depth-averaged flow in the direction of tidal wave propagation or the sea surface elevation over the sand waves.

Our findings demonstrate a clear link between the sand wave field configuration and the resulting form roughness. Sand wave fields oriented obliquely to the dominant flow direction experience increased form roughness. Increasing sand wave height and decreasing wavelength generally lead to higher form roughness according to most criteria. Interestingly, the orientation of a sand wave field impacts roughness differently depending on the latitude, with the Coriolis force playing a significant role.

Notably, for our model configuration, the phase-based criteria are highly sensitive to the starting bathymetric phase (i.e., the sand wave field topography starting between a crest or a trough). This makes the resulting form roughness for the phase-based criteria highly dependent on the specific bathymetry.

This study highlights the limitations of mimicking flow over sand waves with solely roughness adjustments in flat seabed models. While our method does not provide a single, definitive form roughness value due to the varying dependencies observed between each criterion, it offers a valuable approach for incorporating bedform information into model calibration. This approach contributes to a more physics-based representation of roughness compared to current practices.

***Keywords*:** tidal sand waves, sand wave orientation, process-based modelling, form roughness.

Table of Contents

List of figures

List of tables

1 Introduction
1.1 Tidal sand waves
1.1.1 Characteristics and relevance

Tidal sand waves are bed features found in sandy shelf seas with wavelengths spanning from 100 to 1000 meters, a height of several meters (see Figure 1 and Figure 2), and a migration rate of the order of meters per year (van der Meijden et al., 2023; van Dijk & Kleinhans, 2005). Sand waves are formed under the influence of tidal currents. These features generally occur perpendicular to tidal currents, and they can propagate either upstream or downstream with respect to the direction of the residual current (Zhou et al., 2022). In general, environmental conditions such as water depth, flow velocities, and grain size influence the characteristics of sand waves such as their wavelength, wave height, and migration rate (Damen et al., 2018; van der Meijden et al., 2023). Sand waves vary from symmetrical to asymmetrical shapes, with the steeper slope facing the direction of the sand wave propagation (van Dijk et al., 2021).

The significance of sand waves lies in their interaction with various offshore human-related activities, such as submarine pipelines, wind turbines, and navigation. Additionally, they affect the flow and influence sand transport rates, potentially impacting the erosion/accretion dynamics of coastlines (Morelissen et al., 2003; Németh, 2003; Wang et al., 2019).

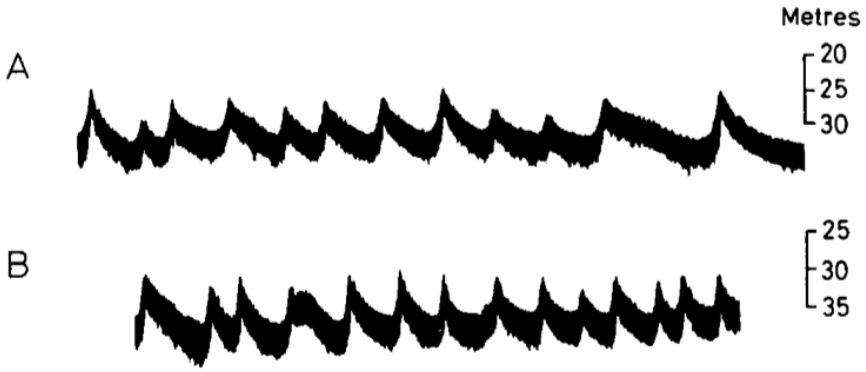

Figure 1 Cross-section of sand waves in the Flanders Bight of the North Sea. Approximate lengths of sections are A = 3800 m and B = 2800 m (McCave, 1971).

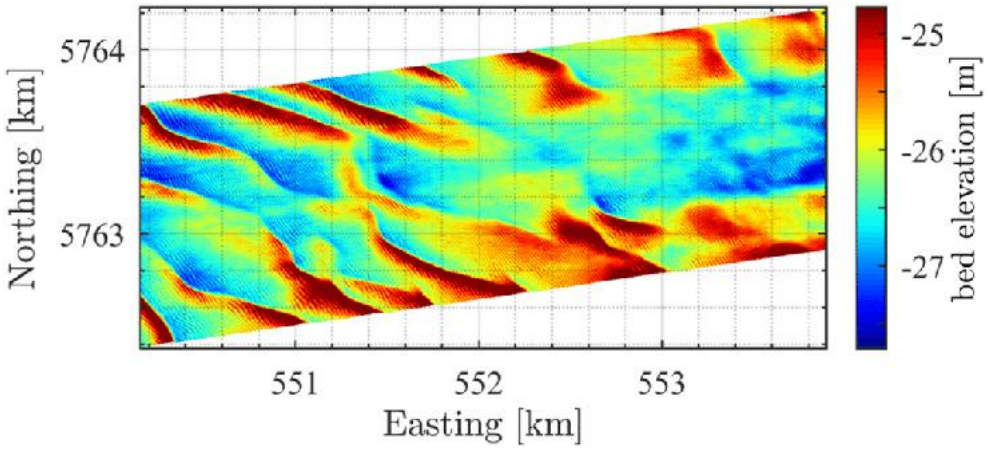

Figure 2 Sand waves in the approach channel to Rotterdam harbor in the North Sea plotted using data from Rijkswaterstaat. The bed elevation is with respect to the lowest astronomical tide (LAT) and coordinates are in UTM, zone 31U (Campmans et al., 2021).

1.1.2 Formation and evolution

Sand waves form due to the inherent instability of a flat mobile seabed subject to tidal flow (Hulscher, 1996). The interaction of the forcing oscillatory tidal current with the seabed perturbations generates steady and harmonic velocity components. This interaction is dependent on hydrodynamic and morphodynamic factors. For some wavelengths of the bottom perturbation, the sediment is consistently transported from troughs to crests by the velocity components (generating steady recirculating cells, see Figure 3), causing the bottom perturbations to grow and resulting in the development of sand waves (Besio et al., 2006, 2008; Hulscher, 1996). This mechanism fosters the further formation and growth of sand waves (Hulscher, 1996).

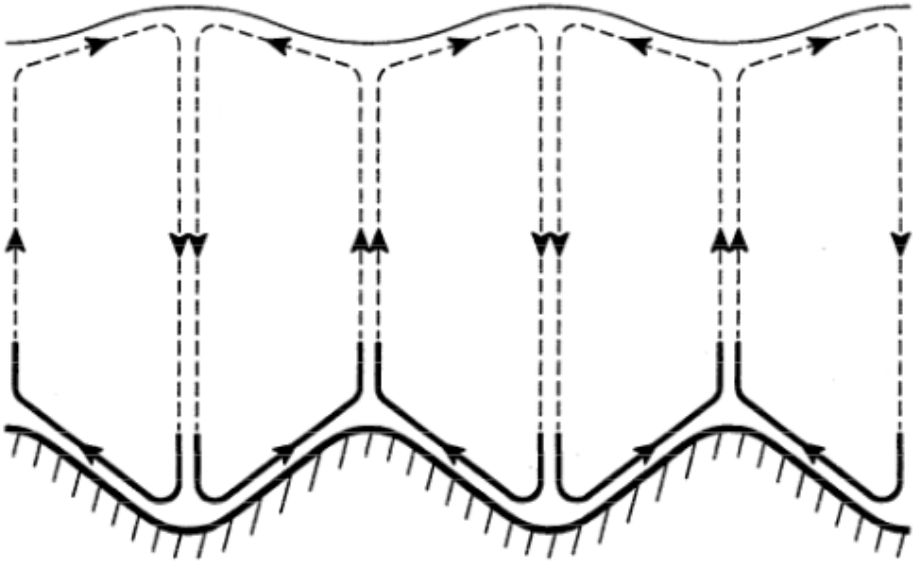

Figure 3 Recirculating cells due to the interaction of a symmetric oscillatory tidal current with sand waves (Hulscher, 1996).

The linear perturbation approach outlined above, initially proposed by Hulscher (1996), explains the formation of sand waves as free instabilities of the morphodynamic system. This approach has been further expanded by the addition of various physical factors such as tidal asymmetry, biota, storms (see Besio et al., 2004; Borsje et al., 2009; Campmans et al., 2017). However, this approach is limited by the assumption of a low-amplitude perturbation (i.e., bedforms have low amplitude compared to the mean water depth) limiting its applicability to the formation stage of sand waves. In addition to linear approaches, nonlinear idealized process-based models have also been used to study nonlinear physical interactions involved in sand wave dynamics. These models allow the analysis of sand waves beyond the formation stage. For instance, Németh (2003) modeled offshore sand waves using a nonlinear model, while Campmans et al. (2018) investigated the nonlinear impact of storms on the evolution of sand waves by modeling their development from a randomly perturbed seabed until reaching an equilibrium shape.

Alternatively, other nonlinear numerical models like Delft3D have also been used to study sand waves. Borsje et al. (2013), investigated the formation of sand waves under the effect of a spatially and temporally variable vertical eddy viscosity model ($k-\varepsilon$ turbulence model). The

study was followed by Borsje et al. (2014), studying the role of suspended load transport in the formation of sand waves, showing that suspended load transport causes suppression of long sand waves, leading to a finite range of wavelengths that experience growth. Van Gerwen et al. (2018) further investigated the role of suspended load transport including tidal asymmetry, showing that both influence the equilibrium sand wave height finding wave heights slightly higher than those found in the field. Damveld et al. (2020) used Delft3D to study the horizontal and vertical sediment sorting processes in tidal sand waves, showing that typically the crest is coarser than the troughs. Krabbendam et al. (2021) set up a calibrated model to study the evolution of sand waves in four transects of the North Sea.

While the previously mentioned studies focused on the morphodynamic evolution of sand waves, less attention has been given to the effects of sand waves on large-scale hydrodynamics. Only a recent study by Portos-Amill et al. (2024) has studied the influence of sand waves in the tidal flow. They investigate the induced form roughness by forcing a propagating M_2 tidal wave over a sand wave field in a 2DV setting.

1.2 Form roughness

1.2.1 General concept

The study by Portos-Amill et al. (2024) is based on the physical concept of shear stress induced by tidal currents on the seabed. Bed shear stress influences sediment transport and sediment grain size distributions (Torres & Uncles, 2011), and is closely linked to bed roughness which represents the extent of frictional resistance exerted by the seabed on the flowing water. Bed shear stress is parametrized as the tangential force per square meter exerted by the fluid on the seabed.

$$\vec{\tau}_b = f\rho_0\vec{u}|\vec{u}| \qquad \text{Eq. 1}$$

where, ρ_0 is the reference density of water, g is the gravitational acceleration, $\vec{u}$ is the depth-averaged flow velocity, and f is a dimensionless friction parameter. In fact, bed shear stress can be estimated based on different coefficients that are used to express bed roughness (e.g., Chézy, Manning); these coefficients are commonly measured empirically (e.g., van Rijn, 1993). For instance, the Chézy coefficient (C) have the physical unit $m^{1/2}\ s^{-1}$ and is related to f, as:

$$C = \sqrt{\frac{g}{f}} \qquad \text{Eq. 2}$$

and the Manning coefficient (n) have the physical unit $m^{-1/3}s$ and is related to f, as:

$$n = H^{1/6}\sqrt{\frac{f}{g}} \qquad \text{Eq. 3}$$

where, H is the mean water depth. Based on any of these parametrizations, the dimensionless roughness parameter f can be used to represent bed roughness.

There are various sources of roughness, including bedforms and grain size. Therefore, to account for these sources, the effective bed roughness (f_{eff}) is generally calculated as the sum of the grain-related roughness (f_g) and the drag on the bed caused by bedforms known as form roughness (f_f), as:

$$f_{eff} = f_g + f_f \qquad \text{Eq. 4}$$

1.2.2 Existing form roughness studies

The complexity of quantifying form roughness is related to the heterogeneity of bedforms in the field (e.g., bedforms can have different characteristics such as height, wavelength, and asymmetry, see Figure 4) and the superimposition of bedforms found in the field (e.g., ripples over a sand wave).

There are several equations used to quantify the roughness caused by different bedforms such as ripples, megaripples, and river dunes (e.g., Soulsby, 1997; Styles & Glenn, 2002; van Rijn, 1993, 2007). For instance, van Rijn's (1993) parametrization for ripple-induced form roughness demonstrated good agreement with measurements taken from the Mississippi River. This parametrization yields a form roughness approximately 10 times larger than grain roughness for typical ripple dimensions. These parameterizations are primarily focused on river studies where the assumptions of steady, unidirectional flow are valid. However, sand waves develop under the influence of tide-dominated dynamics, where those assumptions are no longer valid. Unlike unidirectional flow, tides are characterized by multiple tidal components with different amplitude and phase, adding complexity to their quantification of roughness.

The study by Brakenhoff et al. (2020) on ripples highlights the advantage of using a form roughness calibration method over choosing a constant roughness value (i.e., without any physical information of the system), given that it shows the most accurate prediction of local hydrodynamics. Such method has been presented by Portos-Amill et al. (2024) in a 2DV Deflt3D model and second-order perturbation approach analysis for form roughness induced by sand waves.

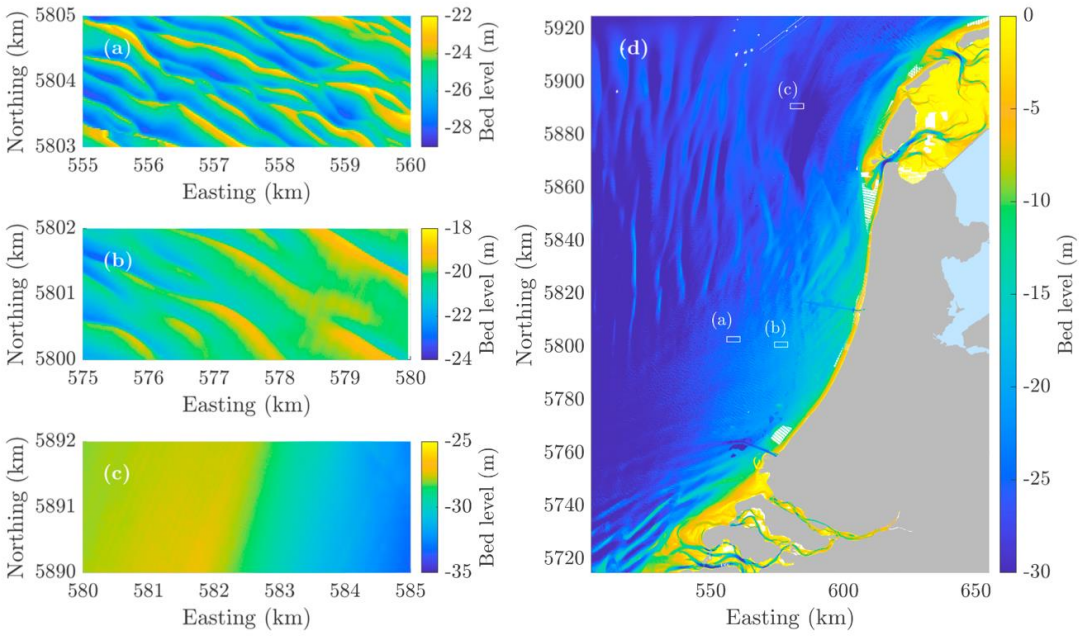

Figure 4 Bathymetric chart of the Netherlands Continental Shelf using data from the Netherlands Hydrographic Service, showing three regions with different bed topography: (a), (b) sand waves with different characteristics, (c) no sand waves (Portos-Amill et al., 2024).

1.2.3 Form roughness of tidal sand waves

Portos-Amill et al. (2024) develop a method in a 2DV setting for assessing the sand wave-induced form roughness, which is part of the bed roughness (see Eq. 4). The findings in Portos-Amill et al. (2024) showed that the presence of sand waves significantly alter various characteristics of tidal flow, such as the amplitude and phase of each tidal constituent. The approach involves comparing the depth-averaged flow or sea surface elevation over a sand wave field (with a grain-induced roughness parameter) to that over a flat seabed with an increased 'effective' roughness (see Figure 5). The method defines form roughness as the additional roughness needed to align the observed amplitude or phase of the depth-averaged flow or sea surface elevation over a sand wave field. This results in roughness values that are amplitude-based and phase-based for the depth-averaged flow and sea surface elevation.

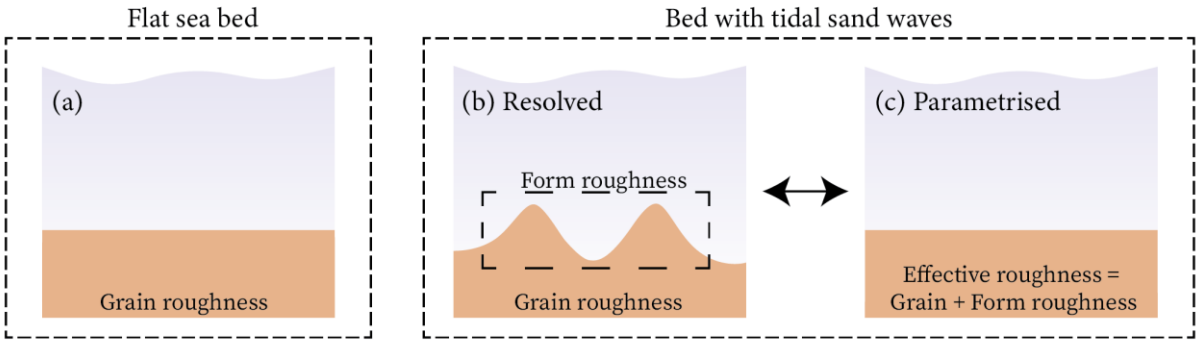

Figure 5 Schematic representation of sand wave-induced form roughness: (a) the roughness that the flow experiences over a flat seabed is purely due to grain roughness. Sand waves add additional roughness to the seabed, which can be modeled either by (b) resolving the sand waves or (c) imposing an increased effective roughness over a flat seabed (retrieved from Portos-Amill et al., 2024).

The resulting form roughness values vary depending on the chosen criteria, highlighting the complex interactions between sand waves and tidal currents. Notably, the form roughness induced by sand waves for some criteria is comparable to grain-induced roughness (i.e., they have the same order of magnitude), emphasizing the crucial role of considering form roughness in large-scale hydrodynamic models where individual sand waves cannot be explicitly resolved due to grid resolution limitations.

1.2.4 Roughness in large-scale hydrodynamic models

In hydrodynamic studies involving sand wave patterns, common engineering practice in modeling (at scales where sand waves are not resolved) is to adjust the effective roughness value as a constant calibration parameter. This adjustment aims to minimize the mismatches between the modeled results and the observations (e.g., water levels, current velocities, morphological changes and so for). The Dutch Continental Shelf Model (DCSM-FM) is a clear example of a model that uses roughness as a calibration parameter (Zijl et al., 2022).

In the DCSM, roughness is calibrated using a Manning coefficient (see Eq. 3), and the final calibration is shown in Figure 6. It can be observed that the calibration has high variations (e.g., a high manning coefficient around relatively lower values) and a seemly arbitrary patchy spatial

pattern. Moreover, the calibration is not based on any physical properties of the system, such as the local characteristics of sand waves (e.g., wave height and wavelength), but is solely adjusted to match the observations of water levels. However, even if the water levels match the observations, there is a mismatch with the calculated and observed flow velocities (Zijl et al., 2022).

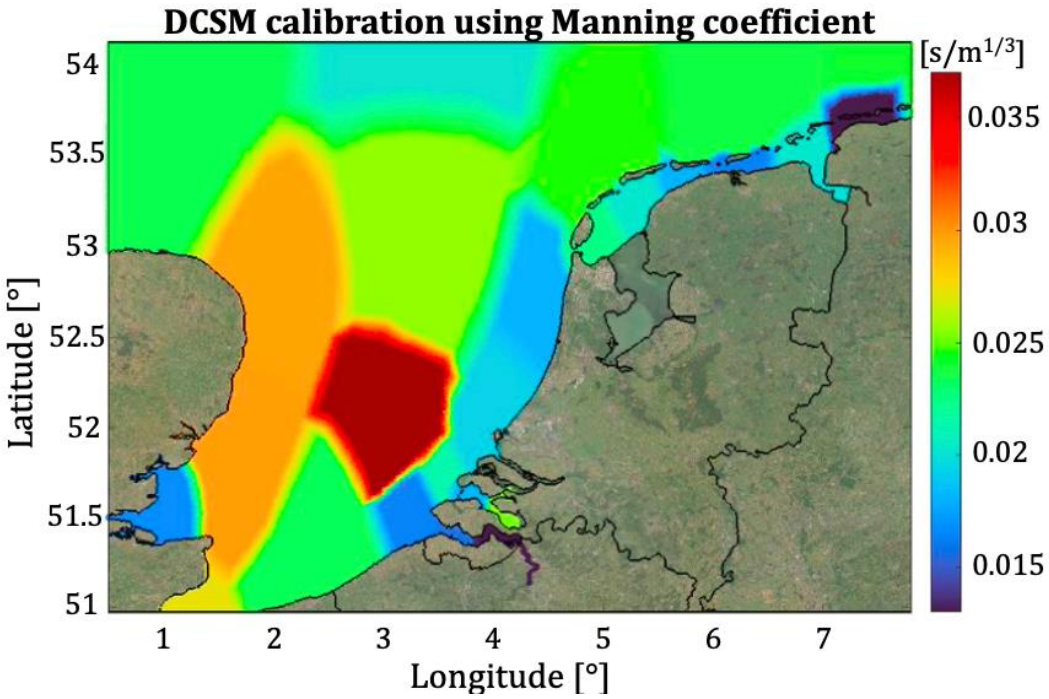

Figure 6 Space-varying bottom roughness field in the DCSM-FM model (modified from Zijl et al., 2022).

1.3 Knowledge gaps

The primary motivation for this research is the lack of physics-based calibration methods for basin-scale tidal flow models. Current practices predominantly focus on matching observed data without considering the underlying physical principles. This lack of a physical background in the calibration process limits the models' accuracy.

Portos-Amill et al. (2024) introduce a method for quantifying form roughness induced by sand waves in a 2DV setting. However, this 2DV approach is inadequate for analyzing key factors such as flow structures in both horizontal directions (in the presence of the Coriolis effect), the distribution of two-dimensional shear stress, and rotated sand wave fields relative to the dominant flow direction. These limitations hinder a comprehensive understanding of the full impact of sand waves on roughness.

1.4 Research objective and questions

Our study aims to analyze the influence of sand wave field orientation relative to the dominant flow direction, as well as various sand wave characteristics (e.g., height, wavelength) on form roughness. Additionally, we want to understand how the presence or absence of the Coriolis force (it allows to investigate the difference between 2DV and 3D setting) affects form

roughness over rotated sand wave fields. By incorporating 3D flow, our research objective is to comprehensively assess the dependence of form roughness on both the characteristics and orientation of sand wave fields.

The scope of the research is limited to sand waves, therefore, excluding other types of marine bedforms such as sand banks, ripples, and megaripples. Additionally, the scope is limited to tidal flow, therefore, excluding waves. Furthermore, the model is set with a fixed morphology since the focus is on examining the impact of sand waves on tidal flow. Consequently, morphodynamics are not within the scope of this project. This exclusion is due to our study being centered on hydrodynamics at tidal timescales (hours, days), while the morphodynamics of sand waves occur over timescales of years.

The main research question of this study is as follows:

What is the influence of sand wave field orientation relative to the dominant tidal flow direction, as well as various sand wave characteristics (e.g., height, wavelength) on the induced form roughness?

From this main research question, three sub-questions are derived:

1. How do the variations in sand wave characteristics (height and wavelength) influence form roughness over a sand wave field perpendicular to the dominant tidal flow direction in the presence of the Coriolis force?
2. How does sand wave orientation influence form roughness in the presence of the Coriolis force?
3. How does the Coriolis force affect the dependency of form roughness on sand wave orientation?

1.5 Thesis outline

The report is structured as follows: Section 2 provides a description of the hydrodynamic model (Delft3D), including a sensitivity analysis of the 2DV model by Portos-Amill et al. (2024), and a description of the 3D model employed in this research. Section 3 presents the results, followed by a discussion of these results in Section 4. Section 5 summarizes the conclusions drawn from this research and Section 6 provides a set of recommendations for future research.

2 Methodology

We have chosen to use Delft3D numerical model to establish our 3D model, expanding upon the model adopted by Portos-Amill et al. (2024). The decision to use Delft3D is based on the advantages it offers over idealized-based models, for example, its capability to incorporate a spatio-temporally varying vertical eddy viscosity. In this section, we provide a brief description of Delft3D in subsection 2.1. In subsection 2.2, we explain the quantification of form roughness in the 2DV setting, followed by subsection 2.3 with a sensitivity analysis of the 2DV model set-up of Portos-Amill et al. (2024) to assess the impact of grid resolution and time step in the results. Next, in subsection 2.4 we present the description of the 3D model presented for this research. Finally, in subsection 2.5, we explain the quantification of form roughness in the 3D setting.

2.1 Delft3D model description

Delft3D is a widely known process-based model developed by Deltares. The model can be used for modeling of coastal, river and estuarine areas in both 2D and 3D settings. Since its development, the Delft3D software contained several integrated modules that allow for the simulation of flow (based on shallow water assumption), short wave generation and propagation, sediment transport, morphological changes, and the modeling of ecological processes and water quality parameters (Lesser et al., 2004). From its early stage, Lesser et al. (2004) showed that the model performs well in several theoretical, laboratory, and real-life situations.

The usability of the Delft3D model comes at the cost of computational effort given the amount of integrated modules a model could run. Several advantages are found in using this model, such as the inclusion of a turbulent eddy viscosity, use of complex bathymetry, and so forth. Thus, the use of such a model proves useful when more computationally efficient models cannot integrate certain features or processes.

There are two versions of Delft3D available: Delft3D-4 and Delft3D FM. For this study, we use the Delft3D-4 model, which employs an Alternating Direction Implicit (ADI) method for the time integration of the shallow water equations. The ADI method also allows a user defined time-step implementation compared to Delft3D FM which uses a time integration based on the advection term and the time step implementation is set automatically.

Delft3D offers two options for vertical schematization: sigma (σ) and Z-coordinate systems. In this study, the sigma coordinate system is employed because it allows for a smooth representation of the topography. Unlike a Z-coordinate system with fixed vertical levels, the sigma system adjusts its vertical grid according to the bottom topography and the free surface (Deltares, 2024). In Delft3D the σ coordinate system is defined as:

$$\sigma = \frac{z - \zeta}{H - h + \zeta} \qquad \text{Eq. 5}$$

where, z is the vertical coordinate in physical space, H is the mean water depth, ζ is the free surface elevation above the reference level (at $z = 0$), and h is the variation in bathymetry with respect to mean water depth. This means that $\sigma = 0$ and $\sigma = -1$ characterize the free surface and the bed, respectively (Figure 7).

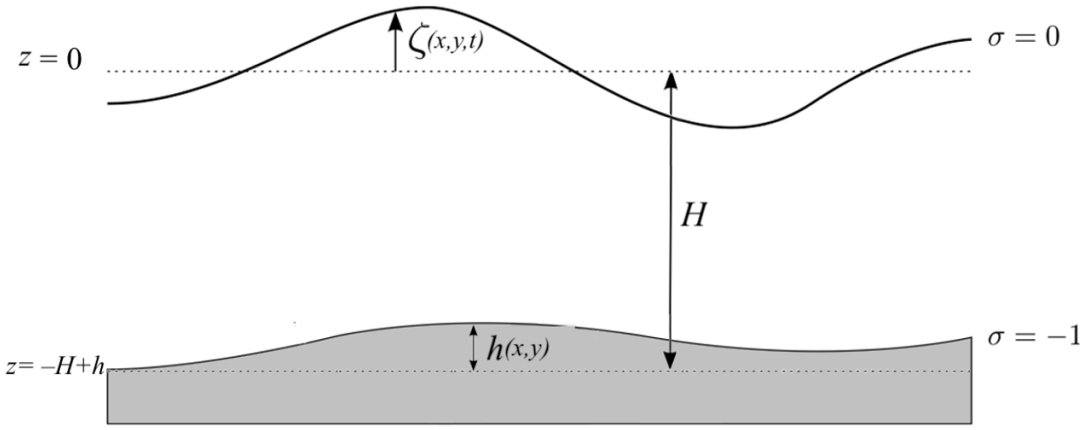

Figure 7 Definition of free surface elevation (ζ), mean water depth (H), and the variations in bathymetry with respect to mean water depth (h) in Delft3D (modified from Deltares, 2024).

Delft3D uses a staggered grid (see Figure 8) for flow calculations. This means that water levels are determined at cell centers, while flow velocities are computed at the grid cell faces. The model solves the shallow water equations, where the vertical accelerations are considered negligible compared to gravity. This simplifies the vertical momentum balance to a hydrostatic pressure relationship. To account for turbulence, the model employs a spatio-temporally varying vertical eddy viscosity (Υ_V). This parameter represents the turbulent mixing within the water column. These simplifications, along with the sigma coordinate system, lead to the following set of simplified 3D shallow water equations:

$$\frac{\partial u}{\partial t} + u\frac{\partial u}{\partial x} + v\frac{\partial u}{\partial y} + \frac{\omega}{H-h+\zeta}\frac{\partial u}{\partial \sigma} - f_{cor}v = -\frac{1}{\rho_w}P_x + F_x + \frac{1}{(H-h+\zeta)^2}\frac{\partial}{\partial \sigma}\left(\Upsilon_V \frac{\partial u}{\partial \sigma}\right) \quad \text{Eq. 6}$$

$$\frac{\partial v}{\partial t} + u\frac{\partial v}{\partial x} + v\frac{\partial v}{\partial y} + \frac{\omega}{H-h+\zeta}\frac{\partial v}{\partial \sigma} + f_{cor}u = -\frac{1}{\rho_w}P_y + F_y + \frac{1}{(H-h+\zeta)^2}\frac{\partial}{\partial \sigma}\left(\Upsilon_V \frac{\partial v}{\partial \sigma}\right) \quad \text{Eq. 7}$$

$$\frac{\partial \omega}{\partial t} = -\frac{\partial \zeta}{\partial t} - \frac{\partial (H-h+\zeta)u}{\partial x} - \frac{\partial (H-h+\zeta)v}{\partial y} \quad \text{Eq. 8}$$

where, u and v are the horizontal velocity in the x and y direction, ω is the vertical velocity in the σ direction, ρ_w is the water density, f_{cor} is the Coriolis force parameter, P_x and P_y are the hydrostatic pressure gradient in x and y direction, F_x and F_y represent the horizontal Reynolds stresses. This study employs a $k-\varepsilon$ turbulence model (which is variable in space and time). This choice is motivated by the demonstrated good agreement between model results employing a $k-\varepsilon$ turbulence model and sand wave field data, as shown by Borsje et al. (2013). This approach outperforms the use of a constant vertical eddy viscosity because it leads to a better approximation of the hydrodynamic aspects. The eddy viscosity resulting from the turbulence model is given by:

$$\Upsilon_V = c_\mu \frac{k^2}{\epsilon} \qquad \text{Eq. 9}$$

where, both the kinetic energy (k) and the energy dissipation (ϵ) are prescribed by a transport equation which is solved to determine the vertical eddy viscosity (Deltares, 2023). The coefficient c_μ is a constant calibration coefficient.

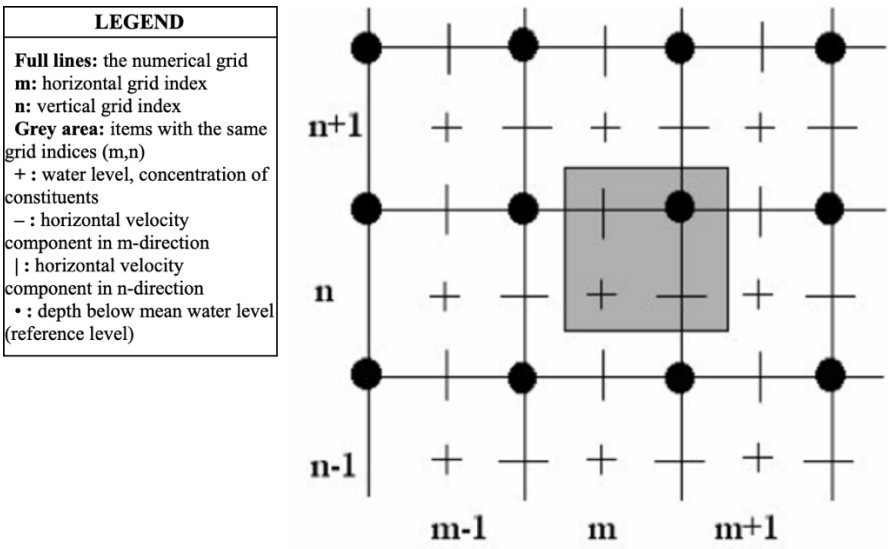

Figure 8 Staggered grid used in Delft3D (Deltares, 2024).

To solve the previously presented simplified 3D shallow water equations (Eqs. 6-8), vertical boundary conditions are defined at the free surface and bed level. Kinematic boundary conditions are applied under the assumption of an impermeable bed and free surface.

$$\omega|_{\sigma=-1} = 0 \text{ and } \omega|_{\sigma=0} = 0 \qquad \text{Eq. 10}$$

These conditions constrain the water movement at the boundaries. Moreover, dynamic boundary conditions, account for the stresses acting at the bed level ($\tau_{b(x,y)}$) and the free surface (τ_s). These stresses influence the water flow within the domain.

$$\frac{v_V}{H-h+\zeta}\frac{\partial u}{\partial \sigma}\Big|_{\sigma=-1} = \frac{1}{\rho_0}\tau_{b,x} \text{ and } \frac{v_V}{H-h+\zeta}\frac{\partial v}{\partial \sigma}\Big|_{\sigma=-1} = \frac{1}{\rho_0}\tau_{b,y} \qquad \text{Eq. 11}$$

$$\frac{v_V}{H-h+\zeta}\frac{\partial u}{\partial \sigma}\Big|_{\sigma=0} = \frac{1}{\rho_0}|\vec{\tau}_s|\cos(\theta) \text{ and } \frac{v_V}{H-h+\zeta}\frac{\partial v}{\partial \sigma}\Big|_{\sigma=0} = \frac{1}{\rho_0}|\vec{\tau}_s|\sin(\theta) \qquad \text{Eq. 12}$$

where, θ is the is the angle between the wind stress vector and the local direction of the gridline. Moreover, Delft3D allows the definition of "land-water" lines, which represent natural boundaries such as riverbanks and coastlines, referred to as closed boundaries. Additionally, it permits the establishment of "water-water" boundaries, referred to as open boundaries. Delft3D allows to set different open boundary conditions related to the sea surface elevation, velocity (in normal direction), discharge, Neumann, and Riemann invariant (Deltares, 2024). Riemann invariants (R) prescribe a linear combination of the horizontal depth-averaged velocity U and the sea surface elevation ζ yielding a propagating tidal wave, expressed as:

$$R_{\pm} = U \pm \sqrt{\frac{g}{H-h}}\zeta \quad \text{Eq. 13}$$

The Riemann type of boundary simulate a weakly reflective boundary (Deltares, 2023), which up to a certain level allows transmission of outgoing waves. Therefore, outgoing waves can cross the open boundary without being reflected into the computational domain as happens for the other types of boundaries.

The bed shear stress is calculated using a formulation for the bed roughness. In Delft3D, the bed roughness can be implemented based on Chézy or Manning employing constant coefficients that may vary spatially (Deltares, 2023). In a 3D setting in Delft3D, depth-averaged calculations often precede 3D calculations for the purpose of calibrating the 3D model. In this context, the shear-stress at the bed induced by a turbulent flow is assumed to be given by a quadratic friction law, as:

$$\vec{\tau}_b = f\rho_0\vec{u}|\vec{u}| \quad \text{Eq. 14}$$

where $|\vec{u}|$ is the magnitude of the depth-averaged flow velocity, f is a dimensionless friction parameter, ρ_0 is the reference density of water, and g is the gravitational acceleration (note that Eq. 1 and Eq. 14 are essentially the same). For this study, we relate the dimensionless roughness parameter f to the Chézy coefficient for implementation in Delft3D (see Eq. 2).

Delft3D uses a time integration of the shallow water equations (Eqs. 6-8) on a rectangular grid based on the ADI method which alternates between explicit and implicit solution techniques applied in both directions of space (i.e., rows and columns) subjected to a time step condition based on the Courant number for wave propagation. Exceeding the time step condition would generate instability (unconditionally stable) and from the view of robustness this is not acceptable (Deltares, 2023). The Courant number and associated Courant conditions are given by:

$$CFL_{wave} = 2\Delta t\sqrt{g(H-h+\zeta)}\sqrt{\frac{1}{\Delta x^2}+\frac{1}{\Delta y^2}} < 1 \quad \text{Eq. 15}$$

where, Δt is the time step, Δx and Δy are the smallest grid spaces in the physical space in its respective coordinate.

2.2 Quantification of form roughness in 2DV

We use the same approach as Portos-Amill et al. (2024) to quantify form roughness. We investigate the impact of sand waves on tidal flow by calculating the magnitude of roughness caused by bedform roughness. The method compares two scenarios: (1) depth-averaged flow in the direction of the tidal wave propagation or sea surface elevation over a sand wave field with a grain-induced roughness parameter (Figure 5b), and (2) a flatbed with an increased "effective" roughness parameter (Figure 5c). Initially, the model resolves the flow over a sand wave field, then iterative runs are conducted with an increased effective roughness over a flatbed to determine the most representative roughness coefficient for the situation that includes the sand waves. Consequently, the difference between the increased effective roughness and the grain-induced roughness yields the form roughness, expressed as follows:

$$f_f = f_{eff} - f_g \quad \text{Eq. 16}$$

where, f_f is the form roughness parameter, f_{eff} is the effective roughness parameter, and f_g is the grain roughness parameter. The grain roughness is $f_g = 2.3 \cdot 10^{-3}$ consistent with Portos-Amill et al. (2024).

Moreover, we apply the same effective amplitude definition as described in Portos-Amill et al. (2024), i.e., half of the difference between the maximum and minimum values of the depth-averaged flow in the direction of the tidal wave propagation (U). Furthermore, the phase is determined from the Fourier transform of U. A similar analysis is also conducted using the sea surface elevation (ζ) instead of U.

2.3 Sensitivity analysis and set-up of the 2DV model

The sensitivity analysis is used to identify optimal configurations for the 3D model, as 3D simulations have higher computational costs. This analysis aims to achieve a balance between computational efficiency and result accuracy. To assess the impact of grid resolution and time step on the resulting form roughness coefficients, we conducted a sensitivity analysis on the 2DV model by Portos-Amill et al. (2024).

The model uses a time step of $\Delta t = 12$ s. Moreover, the model incorporates a static seabed with a central region of $L_{sw} = 2.1$ km containing sand waves (see Figure 9a). This central region is surrounded by flat seabed sections on either side, each extending $L_{flat} = 18.54$ km. The seabed in the model is defined as:

$$z_b(x) = -H + h(x) * Env(x) \quad \text{Eq. 17}$$

where, H is the mean water depth, $h(x)$ is the sand wave topography, and $Env(x)$ is the envelope function. The sand wave topography $h(x)$ profile is defined based on the sand wave height (h_{sw}) and wavelength (λ_{sw}) as follows:

$$h(x) = \frac{h_{sw}}{2} \sin\left(k_{sw}(x - L_{flat})\right) \quad \text{Eq. 18}$$

where, the wave number is defined as $k_{sw} = \frac{2\pi}{\lambda_{sw}}$. The envelope function $Env(x)$ is defined as:

$$Env(x) = \begin{cases} 0 & x \le L_{flat}, \\ \dfrac{1 + \cos\left(\frac{\pi(x - L_{env})}{L_{env}}\right)}{2} & L_{flat} < x \le L_{flat} + L_{env}, \\ 1 & L_{flat} + L_{env} < x \le L_{flat} + L_{sw} - L_{env}, \\ \dfrac{1 - \cos\left(\frac{\pi(x - L_{env})}{L_{env}}\right)}{2} & L_{flat} + L_{sw} - L_{env} < x \le L_{flat} + L_{sw}, \\ 0 & x > L_{flat} + L_{sw}. \end{cases} \quad \text{Eq. 19}$$

where, the transition between the flat seabed and the full-amplitude sand waves is described by a sinusoidal function with horizontal extent of $L_{env} = 100$ m (within L_{sw}). Figure 10 illustrates how this envelope function varies across the model domain. In the sand wave field case, the

roughness applied over the domain is solely the grain-induced roughness (f_g). Conversely, in the flatbed case, the roughness over the model domain is defined as:

$$f(x) = f_g + f_{sw} * Env(x) \qquad \text{Eq. 20}$$

where, f_{sw} represents the increase in roughness for the several simulations used to determine the increased effective roughness (f_{eff}). The roughness profile over a flatbed is illustrated in Figure 9b.

Additionally, the model employs a non-uniform horizontal grid spacing. The grid spacing reaches a maximum value of $\Delta x_{max} = 1542$ m at $x = 0, L$, and progressively decreases to $\Delta x_{min} = 2$ m, which is maintained throughout the sand wave region (see Figure 9c). The thickness of each sigma layer, relative to the local water depth, gradually increases from $5 \cdot 10^{-4}$ at the seabed to $3.28 \cdot 10^{-2}$ at the sea surface.

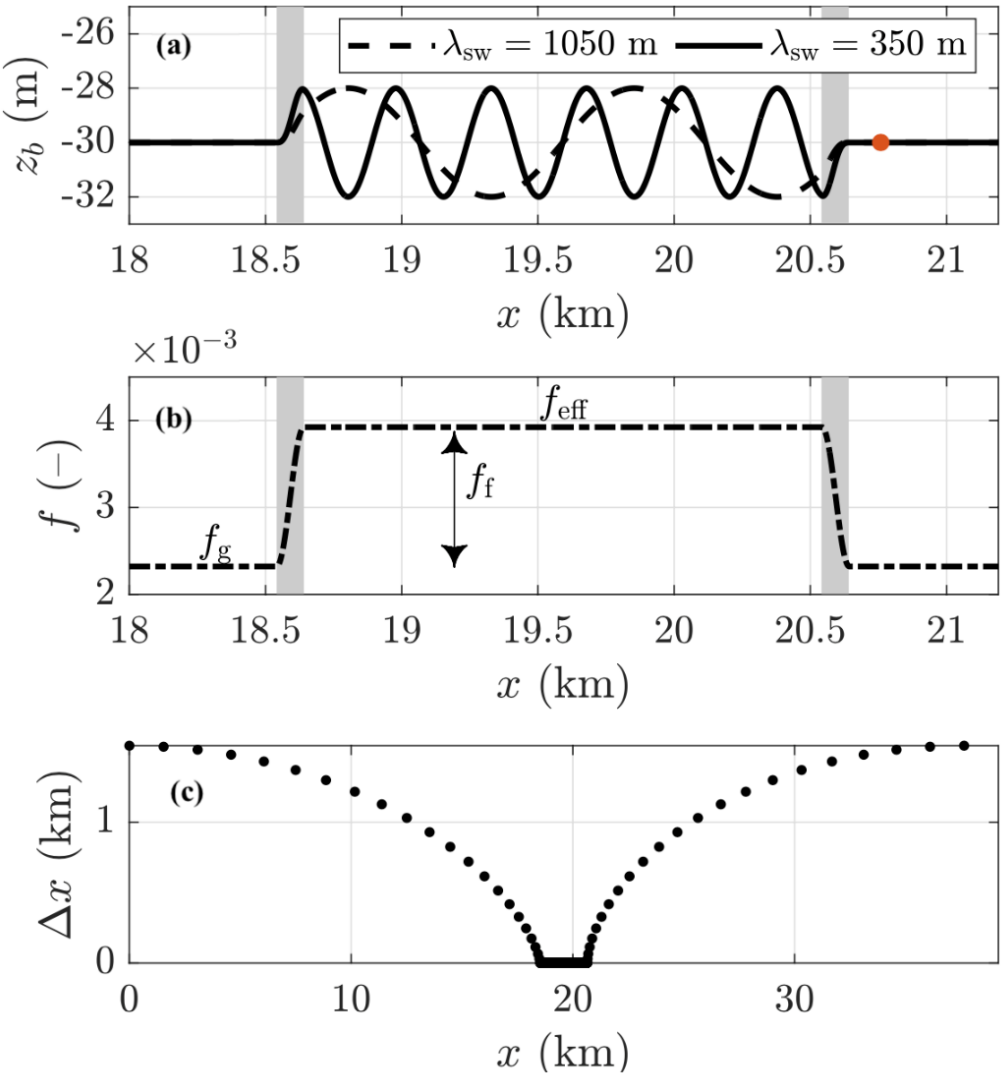

Figure 9 Features of the model: (a) two example bathymetries with different wavelengths used in Delft3D, (b) example of increased friction profile used in Delft3D simulations with a flatbed, (c) horizontal grid spacing Δx used in Delft3D. Note the different x axes in panels (a,b,c). Shaded areas in panels (a,b) denote the envelope regions of length L_{env} where the amplitude of the bathymetry and the friction coefficient change gradually. The red dot in panel (a) is the x-position used in the Delft3D analysis to quantify form roughness as used in the 2DV model of Portos-Amill et al. (2024).

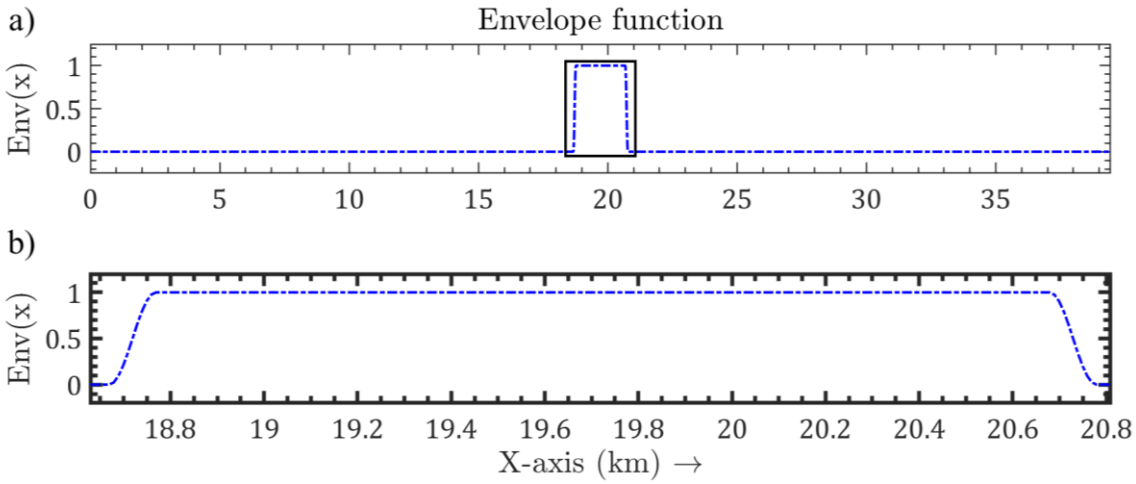

Figure 10 (a) Envelope along the x-axis in the 2DV model. The black box indicates the zoomed-in region in (b).

Moreover, Portos-Amill et al.'s (2024) model incorporates two open boundaries, at $x = 0, L$. At these boundaries, a propagating tidal wave is imposed using Riemann invariants (see Eq. 13). The model is then forced at $x = 0$ by $R_+ = 1.2$ m/s and at $x = L$ by $R_- = 0$ m/s, which results in a propagating tidal wave towards the positive x-direction.

We carried out a sensitivity analysis over a sand wave field with a sand wave height (h_{sw}) of 4 m, sand wavelength (λ_{sw}) of 350 m, and mean water depth (H) of 30 m. The resulting depth-averaged flow in the direction of the tidal wave propagation (U) and sea surface elevation (ζ) are analyzed downwave of the sand wave field or the region with increased effective roughness as shown in the red dot in Figure 9a (see subsection 2.2). For the sensitivity analysis, the finer grid spacing (Δx_{min}) was increased from 2 to $4, 5,$ and 10 m. This coarsening, however, led to significant variations in the calculated effective roughness coefficients, particularly the phase-based values for both U and ζ. This high sensitivity can be attributed to the implicit change in the Courant number (Eq. 15) caused by the grid spacing modification. As the Courant number influences the time step stability of the model, solely refining the grid spacing without adjusting the time step may lead to different behaviors of the model with respect to the base model.

Therefore, a further sensitivity analysis keeping the Courant number constant was carried out. The finer grid spacing (Δx_{min}) was increased from 2 to $4, 5,$ and 10 m and the time step (Δt) was increased from 12 s to 24 s, 30 s, and 60 s, respectively. The computational efficiency is increased by approximately 4, 6, and 25 times compared to the base scenario. A drawback of the model configuration with a grid spacing of $\Delta x_{min} = 4$ m and a time step of $\Delta t = 24$ s is its inability to store results at one-minute intervals. Unlike the other cases, this limitation is imposed by the model's time step. Consequently, the output for this configuration may exhibit lower temporal resolution and potentially interpolation discrepancies compared to the other settings.

The results in terms of U and ζ criteria are presented in Table 1 and the corresponding form roughness coefficients over a flatbed to match the flow over a sand wave field are presented in Table 2. Moreover, U and ζ over a tidal period for the Δx_{min} of $2, 5,$ and 10 m and Δt of 12 s, 30 s, and 60 s are shown in Figure 11 and Figure 12, respectively. The case with Δx_{min} of 4 m

and Δt of 24 s is excluded due to its lower temporal resolution compared to the other configurations. The amplitude-based results show that there is minimal variation for both U and ζ values and their corresponding roughness coefficients. Nevertheless, in terms of the phase-based results, there is a variation of the corresponding roughness coefficient on the order of 10^{-3} for the coarser scenario while for the other scenarios is on the order of 10^{-4}. Considering the efficiency gain and the relatively small phase discrepancies, we opted for a configuration with a grid spacing of $\Delta x_{min} = 10$ m and a time step of $\Delta t = 60$ s for the 3D model. This choice balances accuracy with computational efficiency, as the results remain comparable to the finer scenario.

Table 1 Depth-averaged flow in the direction of the tidal wave propagation and sea surface elevation downwave of the sand wave field for different grid and time step model configurations.

		Depth-averaged flow in the direction of the tidal wave propagation U		**Sea surface elevation ζ**	
Δt (s)	**Δx_{min} (m)**	**Amplitude (m/s)**	**Phase (rad)**	**Amplitude (m)**	**Phase (rad)**
12	**2**	0.5858	0.3013	1.0719	0.2904
24	**4**	0.5857	0.2924	1.0719	0.2815
30	**5**	0.5857	0.3006	1.0718	0.2898
60	**10**	0.5855	0.2994	1.0717	0.2888

Table 2 Corresponding form roughness coefficients over a flatbed to match the depth-averaged flow in the direction of the tidal wave propagation and sea surface elevation either amplitude or phase-based over a sand wave field for different grid and time step model configurations.

		Depth-averaged flow in the direction of the tidal wave propagation U		**Sea surface elevation ζ**	
Δt (s)	**Δx_{min} (m)**	**Amplitude**	**Phase**	**Amplitude**	**Phase**
12	**2**	0.0001	0.0017	0.0001	0.0019
24	**4**	0.0001	0.0020	0.0001	0.0023
30	**5**	0.0001	0.0021	0.0001	0.0024
60	**10**	0.0001	0.0026	0.0001	0.0029

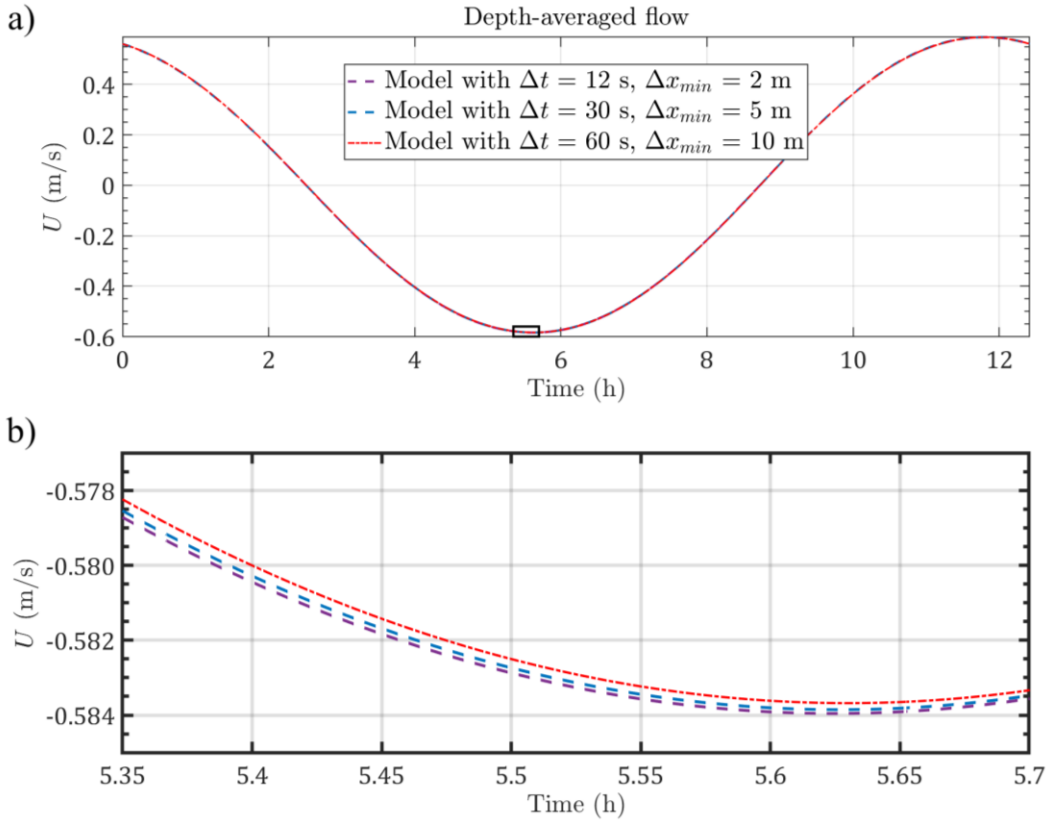

Figure 11 (a) Depth-averaged flow in the direction of the tidal wave propagation over a sand wave field for the different scenarios of the sensitivity analysis. The black box indicates the zoomed-in region in (b).

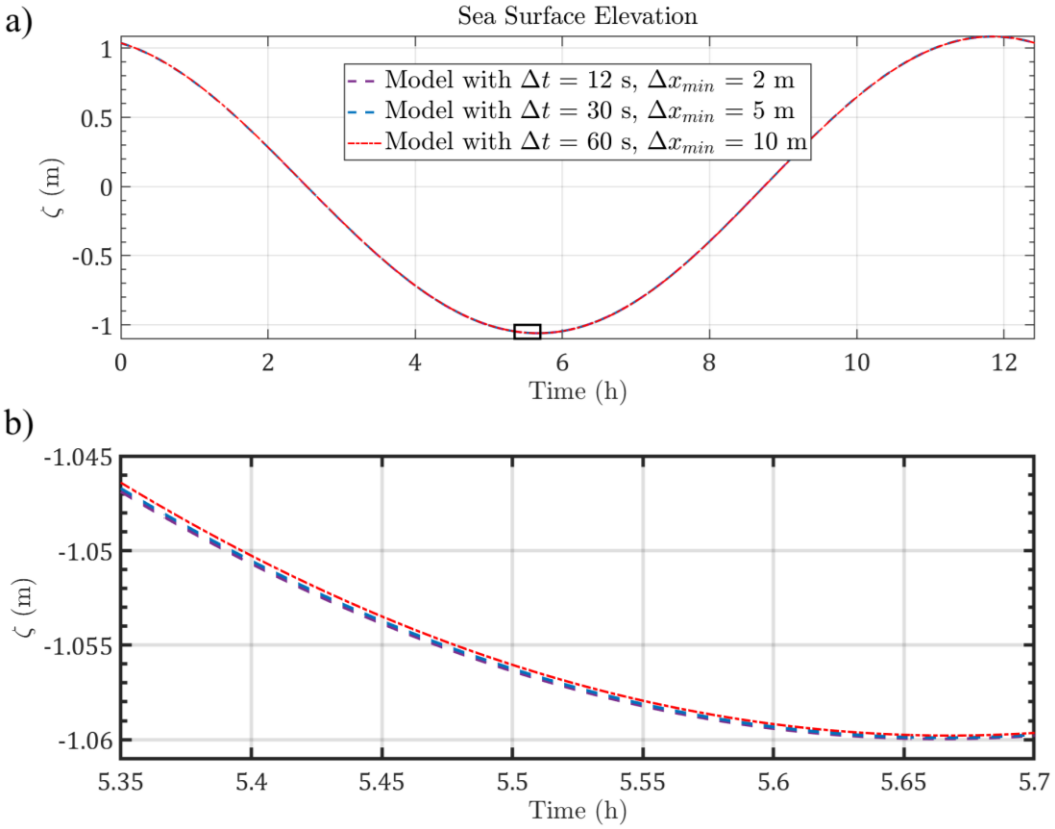

Figure 12 (a) Sea surface elevation over a sand wave field for the different scenarios of the sensitivity analysis. The black box indicates the zoomed-in region in (b).

2.4 3D model set-up

The 2DV model settings by Portos-Amill et al. (2024) are extended to a 3D setting by including the y-coordinate and considering the added features of a 3D model. Firstly, the model grid is coarsened based on the results of the sensitivity analysis (subsection 2.3). Therefore, we used a grid spacing of $\Delta x_{min} = 10$ m and a time step of $\Delta t = 60$ s for the 3D model. This choice balances accuracy with computational efficiency, suitable for the timeframe constraints of this research project. Finer models are highly computationally demanding and require a considerable amount of time.

The model incorporates a static seabed with a central area of $Area_{sw} = 2.1 \cdot 2.1$ km^2 containing sand waves (see Figure 14a). This central area is surrounded by flat seabed sections on all sides, each extending $L_{(x,y)-flat} = 18.54$ km. The seabed in the model is defined as:

$$z_b(x,y) = -H + h(x,y) * Env_{2D}(x,y) \quad \text{Eq. 21}$$

where, $h(x,y)$ is the sand wave topography in the 3D model, and $Env_{2D}(x,y)$ is the 2D envelop function. The sand wave topography $h(x,y)$ is defined similar to the 2DV model (see Eq. 18). To incorporate sand wave orientation, the sand wave field bathymetry is defined as follows:

$$h(x,y) = \frac{h_{sw}}{2}\sin\left(k_{sw}\left[(x - L_{flat})cos(\psi_{sw}) - (y - L_{flat} - \frac{L_{sw}}{2})sin(\psi_{sw})\right]\right) \quad \text{Eq. 22}$$

where, ψ_{sw} is the sand wave orientation, i.e., angle between crest-normal direction and x-axis, with positive angles representing a counterclockwise rotation. The 2D envelope function $Env_{2D}(x,y)$ is defined by multiplying the envelope functions for each direction (x and y), as follows:

$$Env(x) = Env(y) = \begin{cases} 0 & x \le L_{flat}, \\ \dfrac{1 + \cos\left(\frac{\pi(x - L_{env})}{L_{env}}\right)}{2} & L_{flat} < x \le L_{flat} + L_{env}, \\ 1 & L_{flat} + L_{env} < x \le L_{flat} + L_{sw} - L_{env}, \\ \dfrac{1 - \cos\left(\frac{\pi(x - L_{env})}{L_{env}}\right)}{2} & L_{flat} + L_{sw} - L_{env} < x \le L_{flat} + L_{sw}, \\ 0 & x > L_{flat} + L_{sw}. \end{cases} \quad \text{Eq. 23}$$

$$Env_{2D}(x,y) = Env(x) \cdot Env(y) \quad \text{Eq. 24}$$

where, the transition between the flat seabed and the full-amplitude sand waves is described by a sinusoidal function with horizontal extent of $L_{(x,y)-env} = 100$ m (within $Area_{sw}$). Figure 13 illustrates how this envelope function varies across the model domain. Moreover, examples of sand wave fields with different orientation and wavelengths are illustrated in Figure 14.

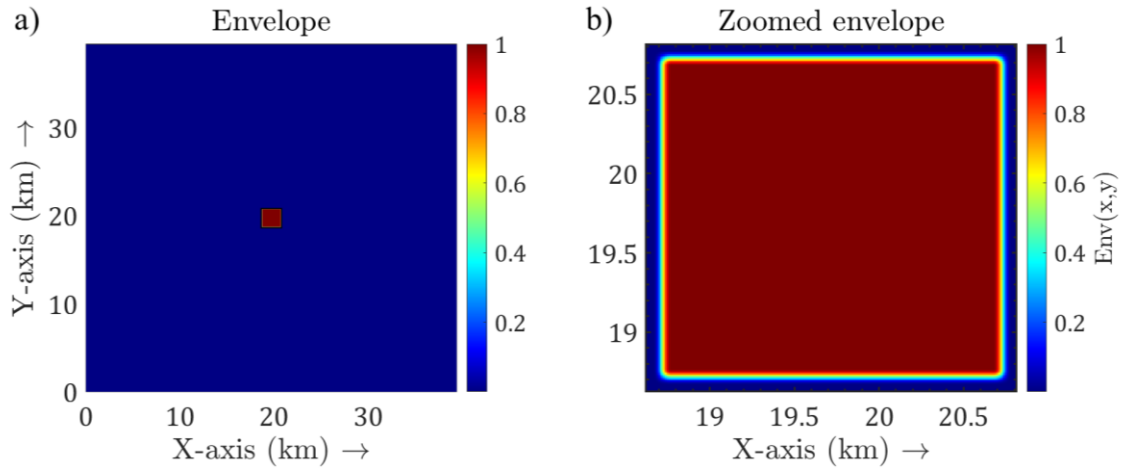

Figure 13 (a) Envelope along the x and y-axis in the 3D model. The black box indicates the zoomed-in region in (b).

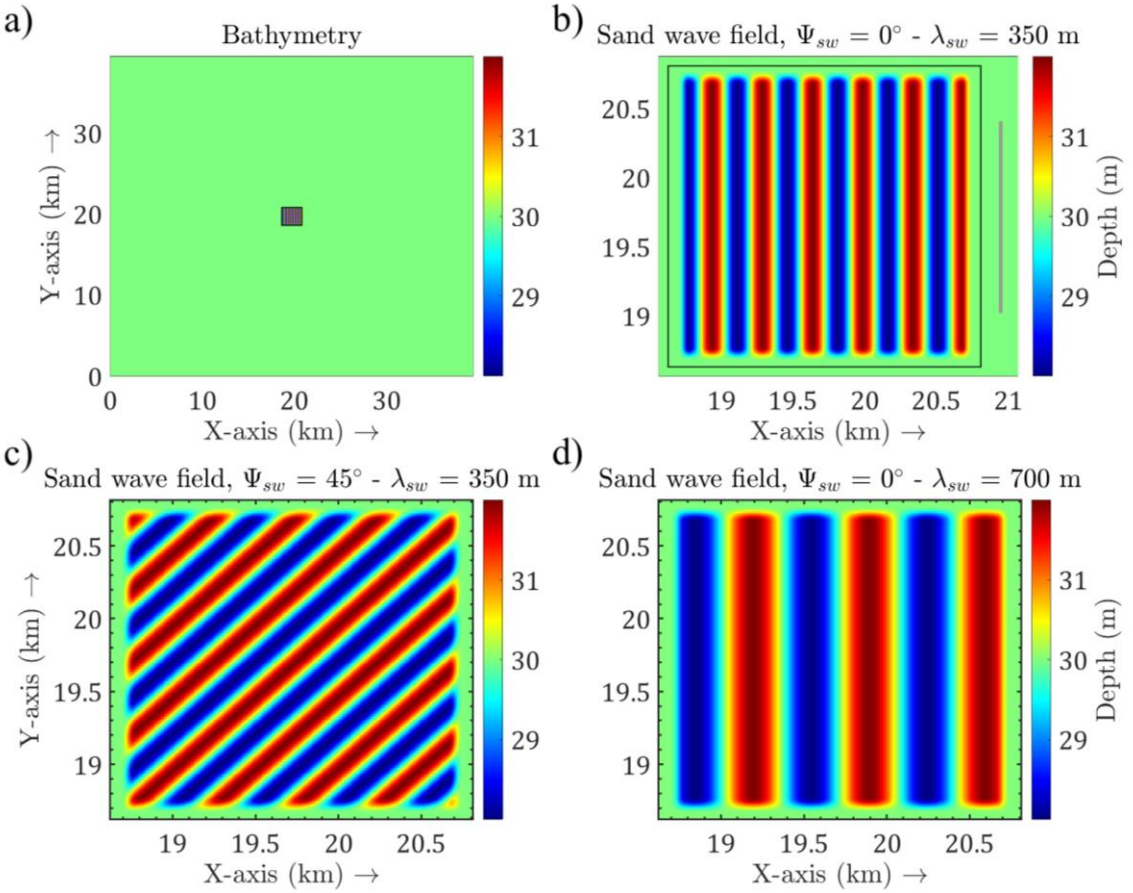

Figure 14 Model bathymetries: (a) Complete model bathymetry with a sand wave field. (b,c,d) Example of three bathymetries with different rotation and phase angles used in the 3D model: (b) $\psi_{sw} = 0°$ and $\lambda_{sw} = 350$ m, showing the x, y-position (grey line) used in the analysis to quantify form roughness. (c) $\psi_{sw} = 45°$ and $\lambda_{sw} = 350$ m. (d) $\psi_{sw} = 0°$ and $\lambda_{sw} = 700$ m. Note that the edges in the bathymetry contain the envelope regions of length L_{env} where the amplitude of the bathymetry changes gradually.

The model employs a non-uniform horizontal grid spacing. The grid spacing reaches a maximum value of $\Delta x_{max} = \Delta y_{max} = 1542$ m and progressively decreases to $\Delta x_{min} = \Delta y_{min} = 10$ m, which is maintained throughout the sand wave region (as shown in Figure 9c and extended in both directions).

We define the default sand wave field with a sand wave height (h_{sw}) of 4 m, sand wavelength (λ_{sw}) of 350 m, mean water depth (H) of 30 m, zero rotation with respect to the horizontal axis ($\psi_{sw} = 0°$). We perform simulations varying the different sand wave field characteristics (h_{sw}, λ_{sw}, ψ_{sw}) from the default sand wave field. The different values used for the different sand wave field characteristics are given in Table 3. The chosen wavelengths ensure that there is always an integer number of sand waves, $N_{sw} \geq 2$, within the sand wave area.

Table 3 Values of the different characteristics used to vary the sand wave topography. The bold values indicate the default case.

Characteristic	**Values**
Sand wave height h_{sw} (m)	1, 2, 3, **4**, 5, 6, 7, 8
Sand wave wavelength λ_{sw} (m)	100, 210, 300, **350**, 420, 525, 700, 1050
Sand wave orientation, i.e., angle between crest-normal direction and x-axis ψ_{sw} (°)	-90, -75, -60, -45, -30, -15, **0**, 15, 30, 45, 60, 75, 90

Moreover, the model incorporates four open boundary conditions, at $x = 0, L_x$ along y and $y = 0, L_y$ along x. At the $x = 0, L_x$ along y boundaries, a propagating tidal wave is imposed using Riemann invariants (see Eq. 13). The model is then forced at $x = 0$ by $R_+ = 1.2$ m/s and at $x = L_x$ by $R_- = 0$ m/s, resulting in a propagating tidal wave towards the positive x-direction. At the $y = 0, L_y$ along x boundaries, a 0 m/s current is imposed to ensure that the fluid velocity is zero at those boundaries, aiding in a more accurate representation of the propagating tidal wave in the model.

Additionally, we also use a $k-\varepsilon$ turbulence model that varies both spatially and temporally. By default, we include the Coriolis force at 52°N (corresponding to the Netherlands) which provides a more accurate representation of a propagating tide in the Netherlands Continental Shelf. Additionally, we also explore scenarios with no Coriolis force and a Coriolis force at 52°S applied to a rotated sand wave field.

In the sand wave field case, the roughness applied over the domain is solely the grain-induced roughness (f_g) for the x- and y-directions. Conversely, in the flatbed case, we implement an isotropic increase of the effective roughness, independent of the angle of rotation (i.e., same increased effective roughness for the x- and y-directions), as follows:

$$f_x(x,y) = f_y(x,y) = f_g + f_{sw} * Env_{2D}(x,y) \qquad \text{Eq. 25}$$

where, f_{sw} represents the increase in roughness for the several simulations used to determine the increased effective roughness (f_{eff}). Figure 15 illustrates an example of the increased friction region as used in the 3D model. The isotropic increase is considered to simplify the model and reduce the number of flatbed simulations.

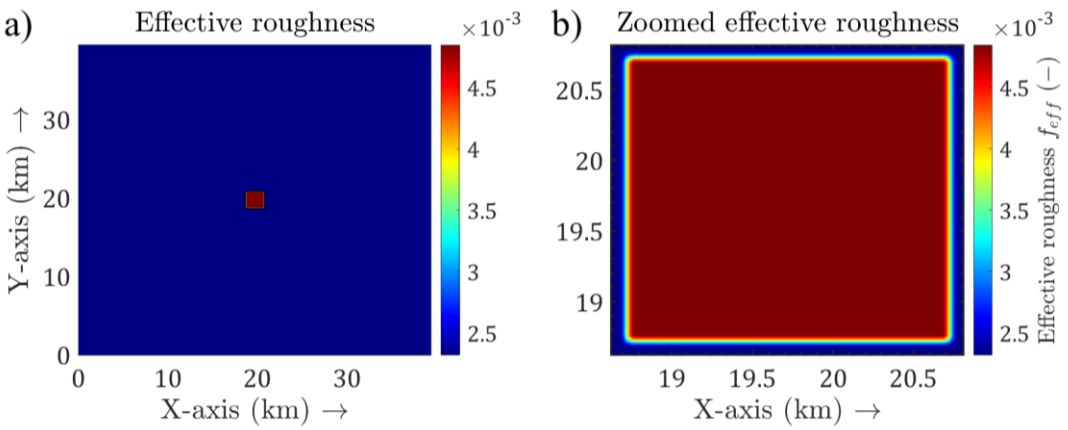

Figure 15 Example of increased friction region used in the 3D model simulations with a flatbed: a) the complete model domain, the black box indicates the zoomed-in region in b). Note that the edges in the increased friction region contain the envelope regions of length L_{env} where the amplitude of the roughness coefficient changes gradually.

2.5 Quantification of form roughness in 3D

We use the same approach as in the 2DV setting to quantify form roughness (see subsection 2.2). Therefore, two cases are compared: (1) depth-averaged flow in the direction of tidal wave propagation (U) or sea surface elevation (ζ) over a sand wave field with a grain-induced roughness parameter, and (2) a flatbed with an increased "effective" roughness parameter. Consequently, the difference between the increased effective roughness and the grain-induced roughness yields the form roughness (see Eq. 16). Moreover, the grain roughness value is the same as in the 2DV setting ($f_g = 2.3 \cdot 10^{-3}$).

Furthermore, we apply the same definition of effective amplitude and phase calculation for the depth-averaged flow in the direction of the tidal wave propagation (U) and the sea surface elevation (ζ) as used in the 2DV setting (see subsection 2.2). The resulting U and ζ are examined downwave of the sand wave field or the region with increased effective roughness. However, in the 3D setting, we consider the space-averaged results (along the y-axis) for U and ζ because focusing solely on a single point downwave of the sand wave field will not capture all the flow differences, particularly in a rotated field. The space-average is calculated at $x = 20.75$ km from $y = 19$ to $y = 20.4$ km (grey line in Figure 14b).

3 Results

We analyze the depth-averaged flow in the direction of the tidal wave propagation (U) and sea surface elevation (ζ) downwave of the sand wave field or the region with increased effective roughness (at $x = 20.75$ km from $y = 19$ to $y = 20.4$ km). Using these results, we determine the effective roughness coefficient (over a flatbed) that best represents the presence of sand waves (see subsection 2.5).

In subsection 3.1, we analyze how the height and wavelength of sand waves influence form roughness over a perpendicular sand wave field in the presence of the Coriolis force. Next, in subsection 3.2, we explore how sand wave orientation influences form roughness in the presence of the Coriolis force. Lastly, in subsection 3.3, we investigate how the Coriolis force affects the dependency of form roughness on sand wave orientation.

3.1 Sand wave characteristics and form roughness

The flow downwave of the sand wave fields with different height and wavelength (see subsection 2.4) is analyzed to study the dependencies between sand wave characteristics and form roughness. Therefore, we use the default sand wave bathymetry ($\psi_{sw} = 0°$) including the Coriolis force at 52°N and varying either the sand wave height or wavelength (see Table 3). Figure 16 presents the resulting form roughness coefficients obtained based on both the amplitude- and phase-based criteria for U and ζ.

Our findings reveal that the ζ-phase-based criterion yields significantly higher form-induced roughness (up to 6 times greater than the ζ-amplitude-based criterion) compared to other criteria (see Figure 16a,b). Furthermore, we observed an increase in form roughness with increasing sand wave height, and a decrease with increasing wavelength, with the exception of the U-phase-based criterion, which shows a peak at $\lambda_{sw} = 700$ m (dashed yellow line in Figure 16b). Interestingly, when the sand wave is high ($h_{sw} = 8$ m) or the sand wavelength is small ($\lambda_{sw} = 100$ m), the form-induced roughness coefficient exceeds the grain-induced roughness coefficient for the ζ-phase-based criterion. Notably, there is no form-induced roughness for the U-amplitude-based criterion, with the exception of the sand wave field with the smaller wavelength. Additionally, it is essential to highlight that the variations in ζ-amplitude and ζ-phase are on the order of 10^{-4} m and 10^{-4} radians, respectively. Still, these small changes lead to significant variations in form roughness (orange lines, Figure 16).

In Appendix A we analyze the impact of a perpendicular sand wave field ($\varphi_{sw} = 0°$) on the cross-tide flow component (V), comparing situations with a sand wave field to those with a flatbed, forced by a propagating tidal wave and the Coriolis force at 52°N. Interestingly, the results show that the presence of a sand wave field perpendicular to the direction of tidal wave propagation does not influence the amplitude of the cross-tide flow component (V) but leads to a phase shift only. Conversely, in the absence of the Coriolis force, there is negligible flow in the cross-tide direction (V) over a perpendicular sand wave field (see Appendix B).

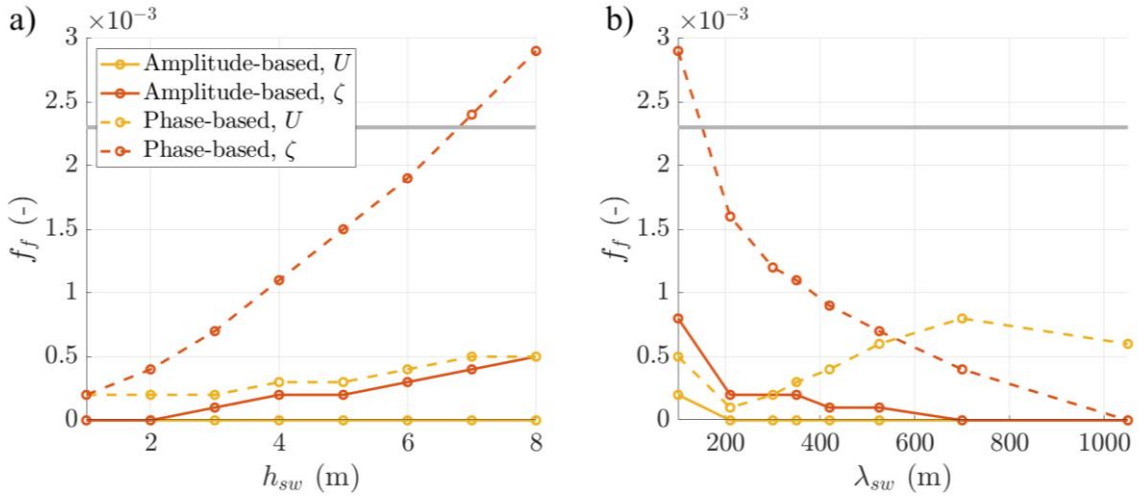

Figure 16 Form roughness (f_f) in terms of (a) h_{sw}, (b) λ_{sw}. The grey line corresponds to the grain roughness (f_g).

3.2 Sand wave orientation and form roughness

This subsection explores the influence of sand wave orientation on form roughness. The orientation is defined as the angle between crest-normal direction and x-axis, with positive angles representing a counterclockwise rotation. We use the default sand wave characteristics ($h_{sw} = 4$ m, $\lambda_{sw} = 350$ m) including the Coriolis force at 52°N latitude and varying the sand wave orientation (see Table 3).

Figure 17 presents the resulting form roughness coefficients obtained based on both the amplitude- and phase-based criteria for U and ζ across a range of rotation angles. It is essential to highlight that the presence of a rotated sand wave field introduces slight variations (of the order of 10^{-2} m) in mean water depth across the simulation domain; however, this minor alteration does not impact the resulting form roughness, as examined in Appendix C.

Our findings reveal a general increase in form roughness when the sand wave field is oblique to the dominant flow direction ($\psi_{sw} \neq \pm 90°$ and $\psi_{sw} \neq 0$). A considerable increase in form roughness for most criteria occurs between 45 and 75 in either direction (i.e., counterclockwise or clockwise), except for the U-amplitude-based criterion (see solid yellow line in Figure 17). Interestingly, when the sand wave field is oriented between 60 and 75 degrees in either direction, the form-induced roughness coefficient exceeds the grain-induced roughness coefficient for the ζ-phase-based criterion.

Additionally, our findings indicate a general maximum form roughness for the ζ-phase-based criterion between 45 and 60 degrees counterclockwise (orange dashed line in Figure 17). Conversely, there is a general maximum for the U-phase-based criterion between 45 and 60 degrees clockwise (yellow dashed line in Figure 17) and for the U-amplitude-based criterion between 15 and 45 degrees clockwise (yellow solid line in Figure 17). Regarding the ζ-amplitude-based criterion, there is an almost symmetric induced form roughness between rotation directions (orange solid line in Figure 17). Notably, the variations in amplitude and phase of ζ are on the order of 10^{-4} m and 10^{-4} radians, respectively. Still, these relatively small changes yield significant variations in form roughness (orange lines, Figure 17).

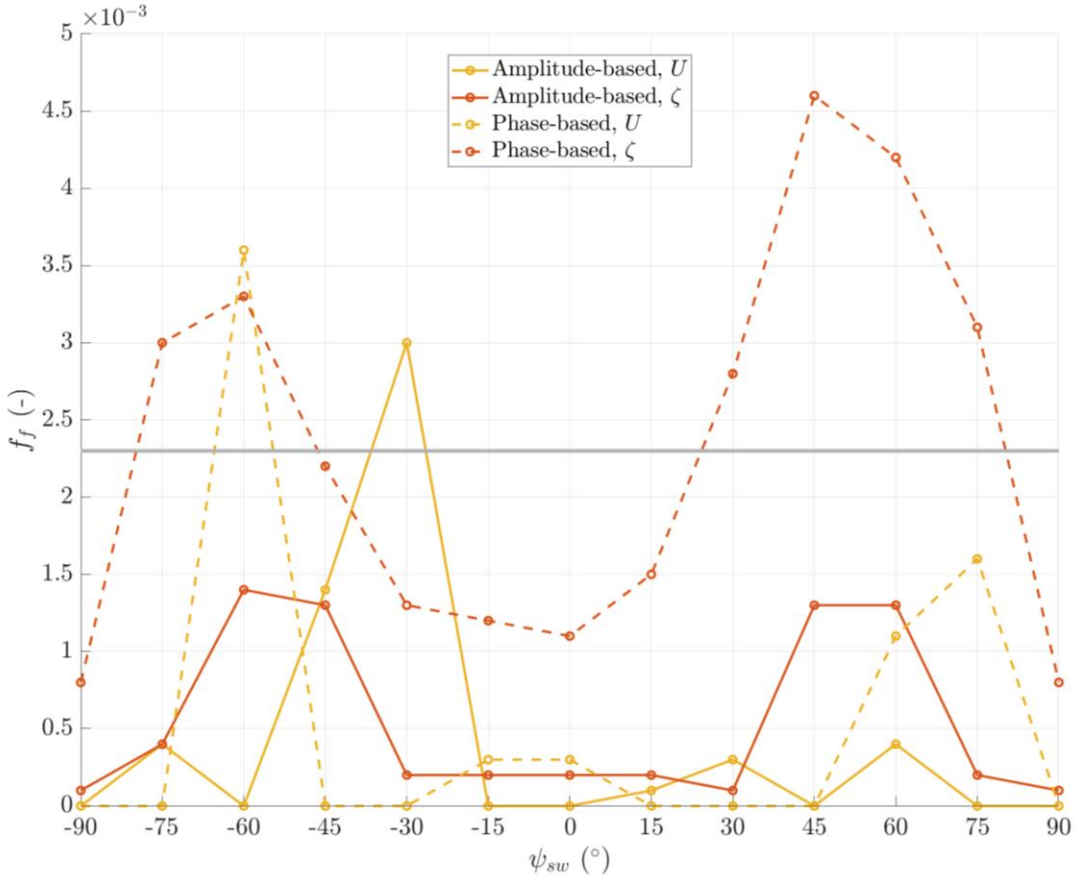

Figure 17 Form roughness (f_f) in terms of ψ_{sw}. The grey line corresponds to the grain roughness (f_g).

3.3 Coriolis influence on sand wave orientation induced form roughness

This subsection explores the interplay between the Coriolis effect and sand wave field orientation in influencing form roughness. We use the default sand wave characteristics ($h_{sw} = 4$ m, $\lambda_{sw} = 350$ m) and incorporate the Coriolis force for scenarios at 52°N, 0°N (no Coriolis) and, 52°S latitudes. Additionally, we vary the sand wave orientation (see Table 3). Figure 18 presents the resulting form roughness coefficients obtained based on both the amplitude- and phase-based criteria for U and ζ across a range of rotation angles under the influence of the Coriolis force at 52°N, 0°N (no Coriolis), and, 52°S latitudes.

Regarding the U criteria, we clearly observe some variations between latitudes at different rotation angles (Figure 18a,b), especially for the U-amplitude-based criterion. For the U-amplitude-based criterion (Figure 18b), there is a higher peak in the Southern Hemisphere than in the Northern Hemisphere and in the absence of Coriolis. These peaks occur when the sand wave field is rotated between 30 and 60 degrees clockwise in the Northern Hemisphere and counterclockwise in the Southern Hemisphere, with peaks at similar orientation angles in either direction in the absence of the Coriolis force. Notably, these peaks in the U-amplitude-based criterion are lower in the absence of the Coriolis effect compared to when the Coriolis force is present. Additionally, induced form roughness for the U-amplitude-based criterion (Figure 18b) in the absence of the Coriolis force and in the Southern Hemisphere occurs when the sand wave

field is rotated between -15 and 15 degrees, whereas, in the Northern Hemisphere there is almost no dependency at these angles of orientation.

For the U-phase-based criterion, our results show an opposite trend compared to the U-amplitude-based criterion. For the U-phase-based criterion (Figure 18a), there is a higher peak in the Northern Hemisphere than in the absence of the Coriolis force and in the Southern Hemisphere. These peaks occur for all latitudes when the sand wave field is rotated between 60 and 75 degrees in either direction, with a higher peak observed in the counterclockwise direction.

Moreover, we observe that the ζ criteria in the Northern Hemisphere (yellow lines in Figure 18c,d) are the mirror image of the ζ criteria in the Southern Hemisphere (orange lines in Figure 18c,d). In the absence of Coriolis, the pattern of the ζ criteria is symmetric between rotation directions (blue lines in Figure 18c,d). Additionally, the ζ-amplitude-based criterion shows a closely similar induced form roughness for all latitudes (Figure 18d), independent of the rotation direction (i.e., counterclockwise or clockwise), and dependent only on the orientation of the sand wave field. There is a peak in the induced form roughness for the ζ-amplitude-based criterion (Figure 18d) between 45 to 60 degrees in both directions.

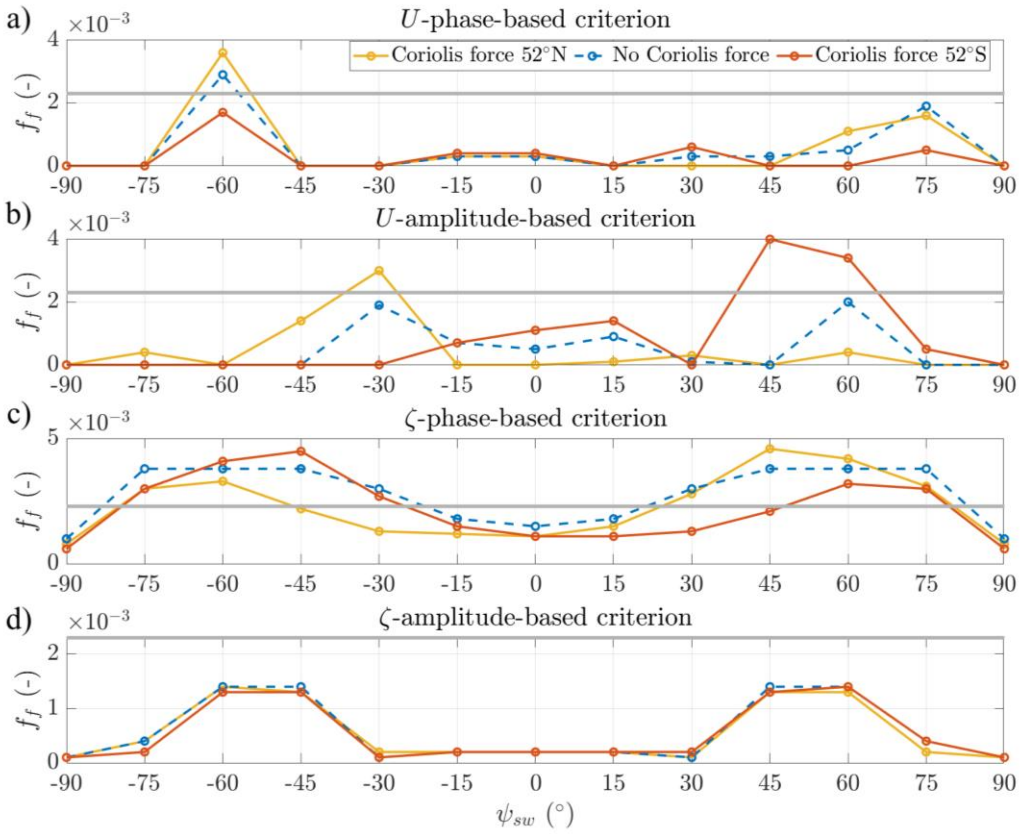

Figure 18 Form roughness (f_f) in terms of ψ_{sw} at 52°N, 0°N, and 52°S latitudes: a) U-phase-based criterion. b) U-amplitude-based criterion. c) ζ-phase-based criterion. d) ζ-amplitude-based criterion. The grey line corresponds to the grain roughness (f_g).

Furthermore, our findings indicate a general maximum form roughness for the ζ-phase-based criterion between 45 and 60 degrees counterclockwise in the Northern Hemisphere (yellow line

in Figure 18c) and clockwise in the Southern Hemisphere (orange line in Figure 18c) due to sand wave orientation. Smaller peaks occur in the opposite direction in both hemispheres. In the absence of the Coriolis force, similar peaks occur between 45 to 75 degrees, regardless of the direction of rotation. These findings suggest that without the Coriolis force, the ζ-phase-based criterion depends solely on the orientation of the sand wave field. However, when the Coriolis force is present, it leads to higher form roughness depending on the hemisphere and rotation direction. It is noteworthy that the variations in amplitude and phase of ζ are relatively small, still, yielding significant variations in form roughness (Figure 18c,d).

Interestingly, our findings show that the form roughness for the ζ-phase-based criterion (Figure 18c) at the peaks (between 45 and 75 degrees in both directions) is comparable to grain-induced roughness (i.e., they have the same order of magnitude). Notably, at the highest peak when the Coriolis force is present (45 degrees clockwise in the Southern Hemisphere and counterclockwise in the Northern Hemisphere), the form induced roughness for the ζ-phase-based criterion doubles the grain-induced roughness (yellow and orange lines in Figure 18c). Moreover, the form roughness coefficients for the U-amplitude-based criterion at the peaks exceed the grain-induced roughness when the Coriolis force is present (yellow and orange line in Figure 18b).

We further analyze how the presence and absence of the Coriolis force affects the variations in the depth-averaged flow components: along-tide (U) and cross-tide (V) across a range of rotation angles.

The change in amplitude for different rotation angles for U and V is illustrated in Figure 19. We observe that the pattern for U-amplitude in the Northern Hemisphere (yellow line in Figure 19a) is partly mirrored in the Southern Hemisphere (orange line in Figure 19a). In the Northern Hemisphere, the U-amplitude decreases between –30 and –60 degrees and increases between 30 and 60 degrees. The opposite occurs in the Southern Hemisphere. In the absence of the Coriolis force (blue line in Figure 19a), there is generally a higher U-amplitude. Unexpectedly, in the absence of the Coriolis force, the U-amplitude exhibits an asymmetric pattern, similar to the pattern observed in the Northern Hemisphere. Notably, the maximum and minimum U-amplitude are highest in the absence of Coriolis and lowest in the Southern Hemisphere, respectively. Interestingly, the U-amplitude is higher over a perpendicular ($\psi_{sw} = 0°$) and parallel ($\psi_{sw} = 90°$) sand wave field in the Northern Hemisphere and in the absence of the Coriolis force compared to the Southern Hemisphere.

For the V-amplitude, the pattern in the Northern Hemisphere (yellow line in Figure 19b) mirrors that of the Southern Hemisphere (orange line in Figure 19b). The results show a peak in V-amplitude at –60 and 60 degrees orientation in the Southern and Northern Hemispheres, respectively. These results suggest that V increases when the sand wave field is rotated clockwise or counterclockwise, suggesting that the Coriolis effect (deflection of winds and currents to the right in the Northern Hemisphere and to the left in the Southern Hemisphere) is enhanced when the tidal flow has a clockwise or counterclockwise orientation relative to the sand wave field, depending on the latitude. Interestingly, the V-amplitude is slightly higher over

a parallel sand wave field ($\psi_{sw} = 90°$) in the Northern Hemisphere compared to the Southern Hemisphere.

Finally, we observe that in the absence of the Coriolis force, the V-amplitude variations are symmetric, with peaks occurring at the same angles as those observed when the Coriolis force is present. However, the V-amplitude in the absence of Coriolis is less than half of what it is when the Coriolis force is present. Especially over a parallel and perpendicular sand wave field, the V-amplitude in the absence of the Coriolis force is in the order of 10^{-3} m/s, which is considerably lower than when the Coriolis force is present (10^{-2} m/s).

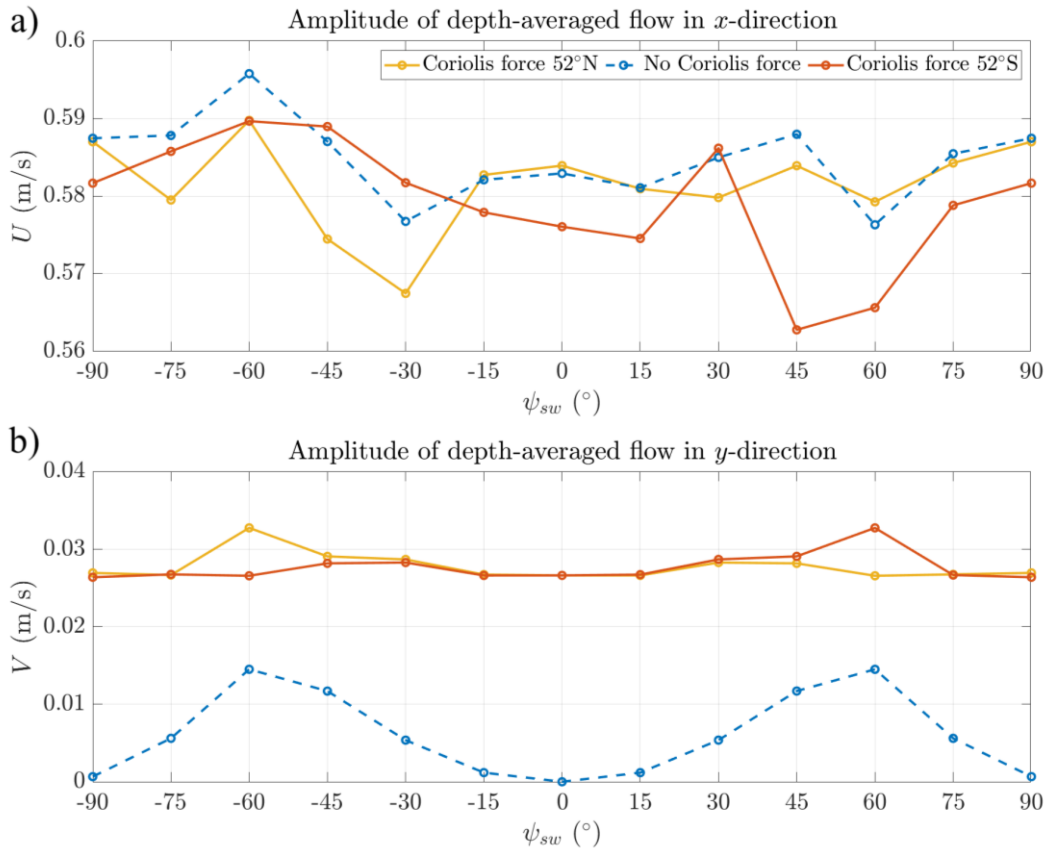

Figure 19 Amplitude change at different rotation angles (ψ_{sw}) at 52°N, 0°N, and 52°S latitudes: a) Amplitude of U. b) Amplitude of V. Note the difference in y-axis.

The change in phase for different rotation angles for U and V is illustrated in Figure 20. The pattern for the U-phase in the Northern Hemisphere (yellow line in Figure 20a) partly resembles the pattern in the Southern Hemisphere (orange line in Figure 20a) and in the absence of the Coriolis force (blue line in Figure 20a). The results show that the U-phase is slightly higher when the sand wave field is rotated between –30 and 30 degrees in the Southern Hemisphere, while for other angles, the U-phase is higher in the Northern Hemisphere and in the absence of the Coriolis force. Interestingly, there is no correlation between U-amplitude (Figure 19a) and U-phase (Figure 20a) across rotation angles.

For the V-phase, the pattern in the Northern Hemisphere (yellow line in Figure 20b) mirrors that of the Southern Hemisphere (orange line in Figure 20b). The pattern in both hemispheres shows only small variations in the V-phase, indicating a relatively minor dependency on the

orientation of the sand wave field. In contrast, the V-phase in the absence of the Coriolis force is highly influenced by the orientation of the sand wave field, showing an asymmetric pattern depending on the direction of rotation. Similar to U, there is no link between V-amplitude (Figure 19b) and V-phase (Figure 20b).

These results highlight a key finding: the variations in both U and V amplitudes and phases are primarily influenced by the sand wave field orientation and the latitude, with no apparent interdependency between both flow components.

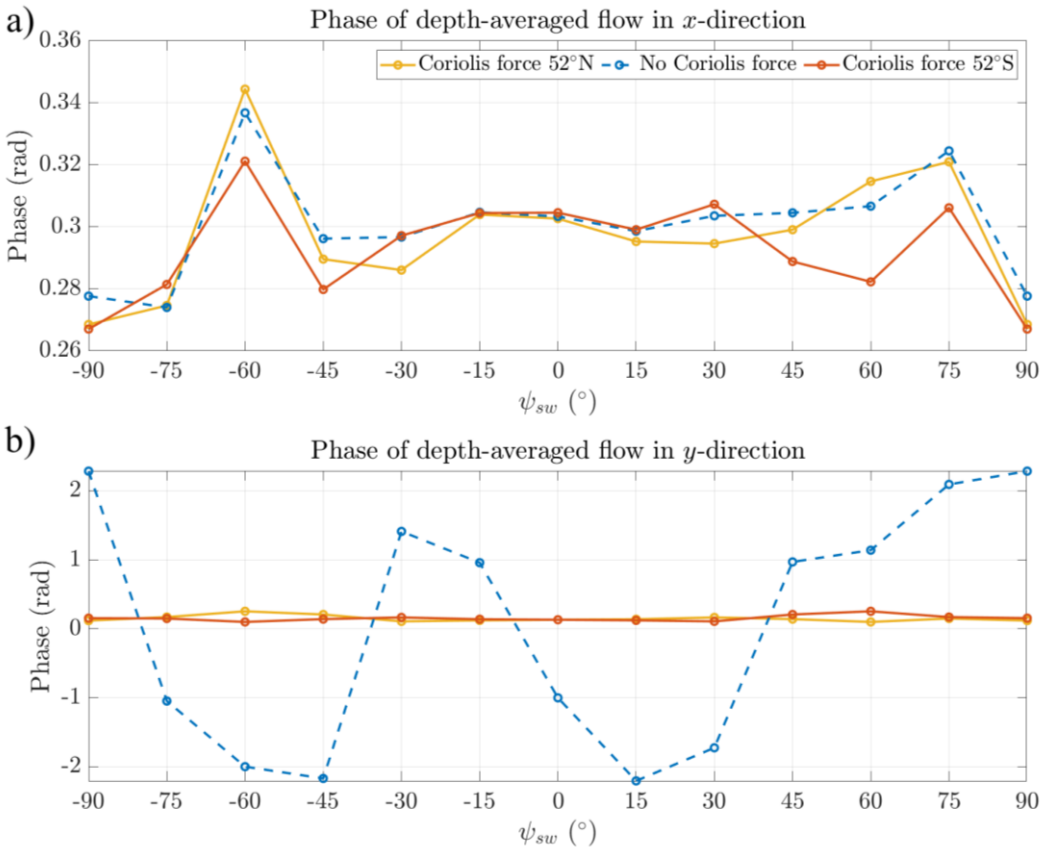

Figure 20 Phase change at different rotation angles (ψ_{sw}) at 52°N, 0°N, and 52°S latitudes: a) Phase of U. b) Phase of V. Note the difference in y-axis.

4 Discussion

This section discusses the key findings presented in Section 3 regarding the influence of sand wave configurations (height, wavelength, and orientation) on form roughness, considering both the presence and absence of the Coriolis force. Firstly, in subsection 4.1 we comment on the robustness of the results. Then, in subsection 4.2 we compare our results with those of Portos-Amill et al. (2024) on sand wave induced form roughness in a 2DV setting. Next, in subsection 4.3 we explore the influence of our chosen model and method settings on the results. In subsection 4.4 we connect our findings to real-world observations of rotated sand wave fields. Finally, subsection 4.5 discusses the practical implications of this study and the method employed.

4.1 Robustness of the results: influence of the bathymetric phase

Following the unexpected results for the different criteria in Section 3, we investigate the model's sensitivity to the sand wave bathymetry. We examine the influence of different phases (ϕ_{sw}) in creating the bathymetry for rotated sand wave fields (i.e., the sand wave field topography starting between a crest or a trough) on form roughness calculations.

$$h(x,y) = \frac{h_{sw}}{2}\sin\left(k_{sw}\left[(x - L_{flat})cos(\psi_{sw}) - (y - L_{flat} - \frac{L_{sw}}{2})sin(\psi_{sw})\right] + \phi_{sw}\right) \quad \text{Eq. 26}$$

where, ϕ_{sw} is the phase of the sand wave topography function. It is essential to mention that all our previous results have been obtained by using a zero phase ($\phi_{sw} = 0°$). An example bathymetry with different phases for a sand wave field rotated 45 degrees is illustrated in Figure 21.

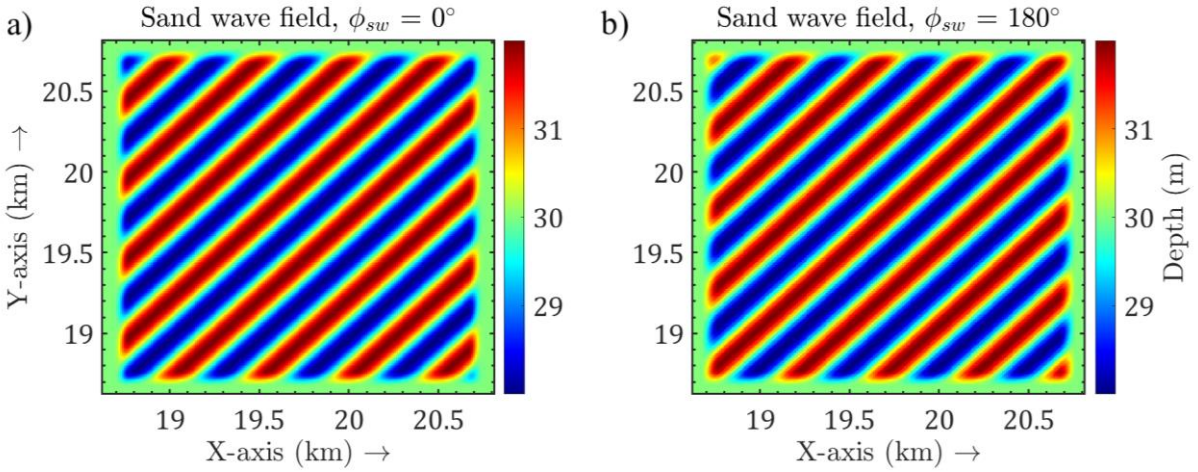

Figure 21 Bathymetries with $\psi_{sw} = 45°$ at different phases: (a) $\phi_{sw} = 0°$, (b) $\phi_{sw} = 180°$. Note that the edges in the bathymetry contain the envelope regions of length L_{env} where the amplitude of the bathymetry changes gradually.

We study two cases: change in phase (ϕ_{sw}) over sand wave fields with (1) different wavelength (λ_{sw}), (2) different orientation (ψ_{sw}). We use the default sand wave height ($h_{sw} = 4$ m) and include the Coriolis force at 52°N latitude. The different values used for the different sand wave field phase are given in Table 4.

Table 4 Values of the bathymetric phase (ϕ_{sw}) used to vary the sand wave topography. The bold value indicates the default case.

	Values
Phase of the sand wave topography ϕ_{sw} (°)	-180, -165, -150, -135, -120, -105, -90, -75, -60, -45, -30, -15, **0**, 15, 30, 45, 60, 75, 90, 105, 120, 135, 150, 165, 180

Figure 22a,b illustrates the form roughness coefficients obtained based on both the amplitude and phase-based criteria for both U and ζ for perpendicular ($\psi_{sw} = 0°$) sand wave fields with different wavelengths across a range of phase angles. The results reveal a clear dependence of the phase-based criteria on the bathymetry phase for perpendicular sand wave fields (dashed lines in Figure 22a,b). This dependence exhibits a sinusoidal pattern, indicating a direct relationship with the bathymetry phase. These results imply that the phase-based criteria are highly sensitive to the specific arrangement of sand waves within the model. In contrast, the ζ-amplitude-based criterion displays minimal variation with changing phase and the U-amplitude-based criterion shows no dependency (solid lines in Figure 22a,b).

Shifting focus to sand wave field orientation, we observe that rotating the sand wave field may result in various configurations depending on the angle (i.e., more crests than troughs or vice versa). Figure 22a,c shows the form roughness coefficients obtained based on both the amplitude and phase-based criteria for both U and ζ for the default sand wave field characteristics oriented at different angles across a range of phase angles. The findings demonstrate that when rotated 45 degrees, only the U-phase-based criterion is affected by the bathymetry phase, unlike the perpendicular case where both phase-based criteria exhibit sensitivity (dashed lines in Figure 22a,c). As observed previously, the amplitude-based criteria display minimal or no dependence on the phase angle for both rotated and perpendicular orientations (solid lines in Figure 22a,c). Interestingly, neither U- nor V-amplitude vary with the change in sand wave field phase in either perpendicular or rotated configurations.

We further analyze the relationship between changes in the phase-based criteria and variations in mean water depth for different phase angles (ϕ_{sw}). Figure 23 illustrates the change in mean water depth across a sand wave field with various characteristics used in this analysis, for different phase angles (ϕ_{sw}).

The results show a clear distinction between the perpendicular (solid yellow and purple lines in Figure 23) and rotated (solid blue line Figure 23) sand wave fields. Perpendicular fields exhibit both a change in mean water depth and a corresponding change in the ζ-phase-based criterion (dashed orange lines in Figure 22a,b). Conversely, the sand wave field rotated 45 degrees displays a constant mean water depth, resulting in no dependence of the ζ-phase-based criterion (dashed orange lines in Figure 22c) on the phase angle. These results suggest that the ζ-phase-based criterion in perpendicular sand wave fields varies with phase due to the fluctuations in mean water depth. However, the consistent change in the U-phase-based criterion across all sand wave fields configurations (dashed yellow lines in Figure 22) suggests it depends solely on the phase angle itself, independent of mean water depth variations.

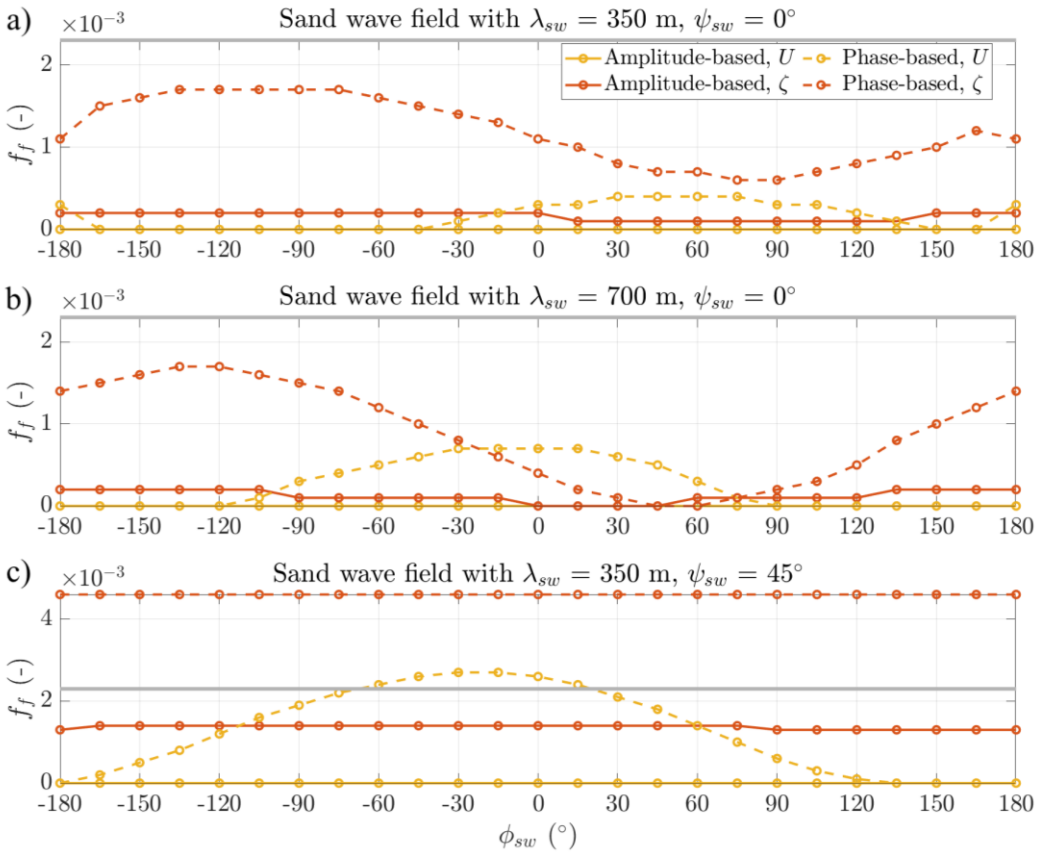

Figure 22 Form roughness (f_f) for a sand wave field with different characteristics across different phase angles (ϕ_{sw}): (a) $\lambda_{sw} = 350\ m - \psi_{sw} = 0°$, (b) $\lambda_{sw} = 700\ m - \psi_{sw} = 0°$, (c) $\lambda_{sw} = 350\ m - \psi_{sw} = 45°$. The grey line corresponds to the grain roughness (f_g).

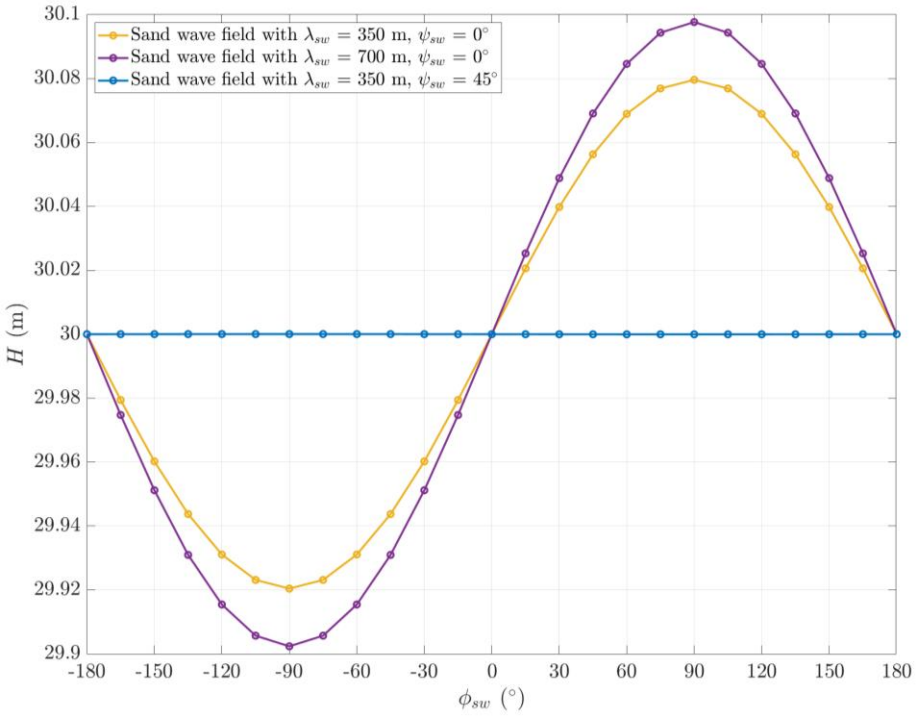

Figure 23 Changes in mean water depth over a sand wave field with different characteristics for different phase angles (ϕ_{sw}).

Our analysis reveals a high sensitivity of the phase-based criteria to the bathymetric phase (i.e., the sand wave field topography starting between a crest or a trough) and the resulting variations in mean water depth. The changes in mean water depth across rotation (ψ_{sw}) and phase (ϕ_{sw}) angles are shown in Figure 24. We observe that the variations in mean water depth for different phase angles are highest for sand wave fields oriented between –15 and 15 degrees. In contrast, for other orientation angles, the change in mean water depth with different phase angles is relatively lower. Therefore, it is essential to be cautious when interpreting form roughness derived from the phase-based criteria, particularly for sand wave fields rotated between –15 and 15 degrees.

In contrast, the amplitude-based criteria exhibited minimal dependence on the bathymetric phase, suggesting greater robustness compared to the phase-based criteria. Notably, the ζ-amplitude-based criterion consistently yielded a clear trend across different model configurations (Coriolis and No-Coriolis). Conversely, the U-amplitude-based criterion exhibited unexpectedly higher peaks for similar scenarios (52°N and 52°S latitude), indicating less consistency.

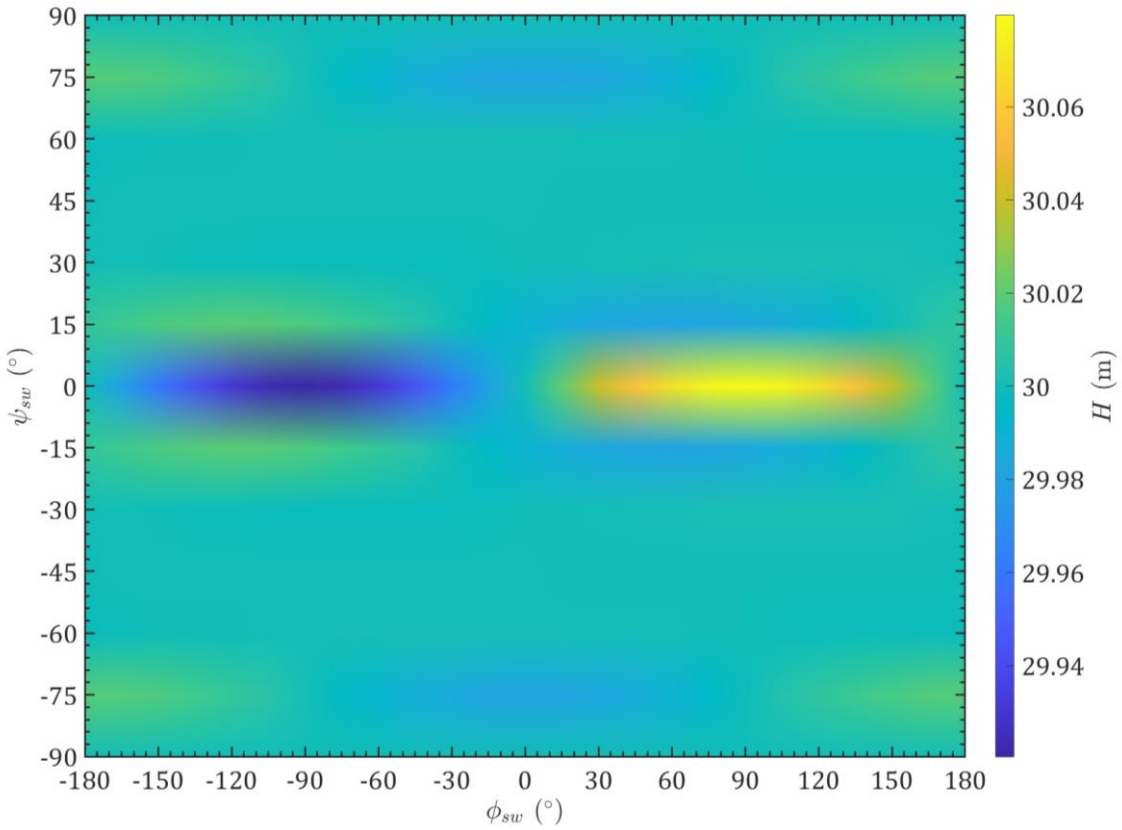

Figure 24 Mean water depth (H) across different rotation (ψ_{sw}) and phase (ϕ_{sw}) angles.

4.2 Comparison with previous studies

We compare our findings on tidal flow over a perpendicular sand wave field with Portos-Amill et al. (2024). It is essential to note that that although both studies employ similar bathymetry definitions, our model uses a coarser grid and incorporates the influence of the Coriolis force at

52°N latitude. This leads to 3D flow structures, absent in the 2DV model of Portos-Amill et al. (2024).

Regarding the flow, our results reveal a decrease in amplitude and a phase shift in the depth-averaged flow in the direction of the tidal wave propagation (U) due to the presence of sand waves (see subsection 3.1). This aligns with Portos-Amill et al.'s (2024) findings in a 2DV setting. In terms of the flow in the cross-tide direction (V), the sand wave field does not influence the amplitude but causes a phase shift only in the presence of a perpendicular sand wave field.

Similar to Portos-Amill et al. (2024), we used four criteria, based on either amplitude or phase, to determine the form roughness that best replicates the observed depth-averaged flow in the direction of the tidal wave propagation (U) or sea surface elevation (ζ) over the sand waves. We found that form roughness increases with increasing sand wave height and decreases with increasing wavelength, except for the U-phase-based criterion (see Figure 16, subsection 3.1). This aligns with Portos-Amill et al. (2024), except for their finding of decreasing form roughness with increasing wavelength for the U-phase-based criterion.

We expected decreasing form roughness dependence on wavelength for the U-phase-based criterion, as it approaches a flat-bed scenario. This change in the U-phase-based criterion, can be explained by the high dependency of the phase-based criteria on the phase (ϕ_{sw}) of the sand wave field bathymetry. Since the results of Portos-Amill et al. (2024) align more closely with our expectations, we hypothesize that this high dependency on the phase of the sand wave field bathymetry is associated with coarsening the grid resolution in our 3D model. However, this should be further studied in a 2DV setting to determine whether this dependency also arises with a finer grid.

Finally, our form roughness values for different sand wave characteristics differ quantitatively from those of Portos-Amill et al. (2024). Particularly for the ζ-phase-based criterion in which Portos-Amill et al. (2024) obtained values between $f_f = 0.2 \cdot 10^{-3} - 8 \cdot 10^{-3}$ which are twice as high as ours for increasing wave height ($f_f = 0.2 \cdot 10^{-3} - 3.8 \cdot 10^{-3}$). This discrepancy is attributed to the presence of the Coriolis force in our model. We observed that in the absence of the Coriolis force, the resulting form roughness for the ζ-phase-based criterion is highest over a perpendicular sand wave field.

4.3 Model and method settings

Our study employed an isotropic increase of the effective roughness (i.e., same increased effective roughness for the x- and y-directions) for computational efficiency, potentially underestimating the impact of rotation-induced form roughness. A better understanding of induced form roughness over a rotated sand wave field could be achieved using an anisotropic approach based on the sand wave field's orientation. While Delft3D allows the incorporation of different roughness values in both directions, time constraints limited this exploration.

Additionally, we observed differing amplitude and phase for the depth-averaged flow in the direction of tidal wave propagation (U) between the 3D model without Coriolis and the 2DV model over a perpendicular sand wave field. We expected these parameters to be similar between the 3D model without Coriolis and the 2DV model. This discrepancy likely arises from the open boundary conditions at $y = 0, L_y$ in the 3D model, which are not present in the 2DV model. While different boundary conditions can affect the resulting form roughness, using a larger model domain could reduce their influence on the results.

Our observations of the criteria over a rotated sand wave field in the absence of the Coriolis force revealed unexpected patterns. We initially expected a symmetrical response regardless of the rotation direction (counterclockwise or clockwise). However, due to the Blackbox nature of Delft3D, identifying the exact cause of this discrepancy is challenging. Employing an idealized model, such as a 3D second-order perturbation approach, could provide deeper insights into the relationships between the rotated sand wave field and the flow dynamics.

Due to time and storage limitations, data collection focused on a single downstream location ($x = 20.75$ km from $y = 19$ to $y = 20.4$ km). While collecting data for the entire domain would be ideal, this limitation restricts our ability to fully understand how the chosen location might influence the derived form roughness.

Finally, we used four criteria (amplitude-based and phase-based) to determine the roughness that matches the depth-averaged flow in the direction of tidal wave propagation (U) and sea surface elevation (ζ) over a sand wave field. However, different dependencies were observed for both flow components: along-tide (U) and cross-tide (V) over a rotated sand wave field in the presence of the Coriolis force. While implementing another criterion for the cross-tide component might introduce additional complexity in selecting the best roughness coefficient, it is essential to recognize that a single value is insufficient to fully represent the flow over a rotated sand wave field. These contrasting dependencies highlight the inherent complexity of quantifying form roughness in a tidal setting.

4.4 Connection with observed sand wave fields

Belderson et al. (1982) observed that in the Bristol Channel (England), sand wave crests deviate slightly (up to 15 degrees) from the peak tidal current direction, exhibiting a counterclockwise rotation (Figure 25). Moreover, Tobias (1989) observed that offshore sand wave crests in the Netherlands are perpendicular to the peak tidal flows, while sand wave crests near the Dutch coast are oriented with an angle of 20° with respect to the peak tidal currents.

The results from simulating a sand wave field rotated 15 degrees anticlockwise (relative to the crest-normal direction and x-axis) under the influence of the Coriolis force at 52°N latitude show an increase in form roughness for the ζ-phase-based criterion, compared to a perpendicular orientation. Nevertheless, the amplitude-based criteria remained similar for both orientations. Notably, the amplitude of both flow components U and V remained similar for the 15-degree counterclockwise orientation compared to perpendicular flow. While Tobias (1989) does not specify the direction of rotation, the results are partly consistent for either direction. It

is important to note that these observations are specific to 52°N latitude. Therefore, including the Coriolis force in the simulations provides more representative results.

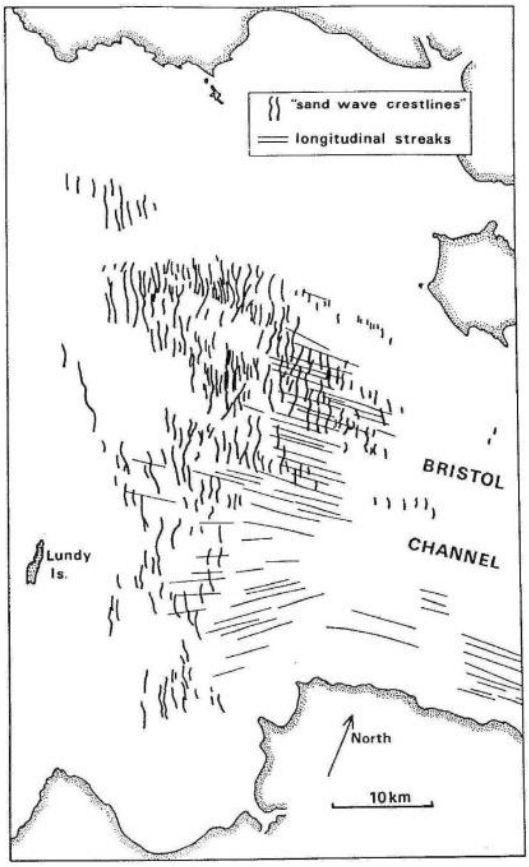

Figure 25 Orientation of sea surface features in the outer part of the Bristol Channel, England, taken from a Seasat side-scan radar image. The sand wave crest orientations vary from about normal to a maximum angle of about 15° to the direction of peak tidal currents, as indicated by the longitudinal streaks on the water surface. Where not normal to the tidal currents, the sand wave crests are rotated in counterclockwise sense relative to the tidal current (Belderson et al., 1982).

4.5 Practical relevance

The common engineering practices in hydrodynamic modeling (at scales where sand waves are not resolved) with respect to the effective roughness is to adjust its value as a constant calibration parameter. This approach aims to minimize discrepancies between model results and observations (e.g., water levels, current velocities, morphological changes and so for). The Dutch Continental Shelf Model (DCSM-FM) for the North Sea exemplifies this practice (Zijl et al., 2022). However, due to this calibration approach, the roughness coefficients used within the model have large variations (e.g., high coefficients around relatively lower values) and cannot properly reproduce the observed flow velocities. Thus, solely calibrating a model to match observations may be insufficient to accurately mimic the complex flow patterns over a sand wave field.

While our proposed method does not determine a definitive form roughness value and is sensitive to the phase of the bathymetry, it offers a way to incorporate bedform-related information into the calibration process. This leads to a more physics-based representation of roughness compared to current practices.

There are some practical considerations for using our method. The observed variations in form roughness coefficients across different criteria underscore the importance of selecting an appropriate criterion (whether amplitude-based or phase-based, to match depth-averaged flow in the direction of tidal wave propagation U or sea surface elevation ζ) to guide the calibration. Given the high sensitivity of the phase-based criteria and the bathymetric phase, it is recommended to be cautious when interpreting form roughness derived from these criteria. Additionally, the presence or absence of the Coriolis force in the model influences the resulting roughness. Therefore, the choice between 2D and 3D calibration settings, particularly for flow perpendicular to the sand wave field, should be based on the desired processes in the model (e.g., including or excluding the Coriolis force).

5 Conclusions

The aim of this thesis was to analyze the influence of sand wave field orientation relative to the dominant flow direction, as well as various sand wave characteristics (e.g., height, wavelength) on form roughness. We used Delft3D numerical model to resolve the hydrodynamics over a sand wave field in a morphostatic setting. To quantify form roughness, we used four criteria, either amplitude-based or phase-based, to determine the roughness that matches the depth-averaged flow in the direction of the tidal wave propagation or sea surface elevation over a sand wave field. These criteria account for the complex nature of tidal flow, composed of various tidal constituents with distinct amplitudes and phases.

We proposed three research sub-questions: (1) how do the variations in sand wave characteristics (height and wavelength) influence form roughness over a sand wave field perpendicular to the dominant tidal flow direction in the presence of the Coriolis force?, (2) how does sand wave orientation influence form roughness in the presence of the Coriolis force?, (3) how does the Coriolis force affect the dependency of form roughness on sand wave orientation?

The results from the model and the resulting form roughness for the four criteria aid us to answer our research sub-questions:

(1) An increase in sand wave height results in an increase in form roughness, while an increase in wavelength results in a decrease in form roughness over a sand wave field perpendicular to the flow, with the exception of the U-phase-based criteria. These findings align with those reported by Portos-Amill et al. (2024), except for the U-phase-based criteria.

(2) A sand wave field oblique to the dominant flow direction ($\psi_{sw} \neq \pm 90°$ and $\psi_{sw} \neq 0$) yields an increase in form roughness. Most criteria show a significant increase in form roughness between 45 and 75 degrees in either direction (counterclockwise or clockwise), except for the U-amplitude-based, which shows an increase at different angles. Notably, when the sand wave field is oriented between 60 and 75 degrees in either direction, the form-induced roughness coefficient exceeds the grain-induced roughness coefficient for the ζ-phase-based criterion.

(3) The obliqueness of a sand wave field increases form roughness independently of latitude. There is a general maximum form roughness for the ζ-phased-based criterion between 45 to 60 degrees counterclockwise in the Northern Hemisphere and clockwise in the Southern Hemisphere. In the absence of the Coriolis force, the ζ-phased-based criterion exhibits symmetrical form roughness regardless of the direction of rotation. The ζ-amplitude-based criterion shows a similar pattern independently of the latitude. For the U-phase-based criterion, a similar pattern exists across all latitudes, with some variations in the induced form roughness at the peaks. The U-amplitude-based criterion shows peaks when the sand wave field is rotated between 30 and 60 degrees clockwise in the Northern Hemisphere and counterclockwise in the Southern Hemisphere, with smaller peaks occurring at the same angles in both directions in the absence of the Coriolis force. These differences in peak form roughness and the direction of orientation highlight the influence of the Coriolis force depending on the sand wave field's

orientation. In general, higher form roughness is observed in the Northern Hemisphere is observed when the sand wave field is rotated counterclockwise for the ζ-phase-based criterion and lower form roughness for the U-amplitude-based criterion, with the opposite trend in the Southern Hemisphere. In the absence of the Coriolis force, a lower influence is observed for these criteria when the sand wave field is oblique.

Combining the results from these sub-questions, we answer the main research question of this study: What is the influence of sand wave field orientation relative to the dominant tidal flow direction, as well as various sand wave characteristics (e.g., height, wavelength) on the induced form roughness?

- A sand wave field oblique to the dominant flow direction yields an increase in form roughness. Increasing sand wave height and decreasing wavelength result in higher form roughness. The Coriolis force contributes to higher form roughness in the Northern Hemisphere when the sand wave field is rotated counterclockwise for the ζ-phased-based criterion and lower form roughness for the U-amplitude-based criterion, with the opposite trend in the Southern Hemisphere. At the equator (no Coriolis force), a lower influence is observed. There is a similar pattern in the form roughness dependency for the ζ-amplitude-based and U-phased-based criteria, regardless of the latitude. It is essential to highlight that under the influence of the Coriolis force, both the orientation and the Coriolis effect are important in quantifying form roughness.

The presented method utilizes phase-based criteria which are highly sensitive to the changes in mean water depth and the bathymetric phase of the sand wave field. These criteria vary sinusoidally with changing phase angles, indicating a strong dependence on the bathymetry itself. Conversely, the amplitude-based criteria exhibit minimal to no such dependence. Therefore, users of this method should be aware of this significant sensitivity in the phase-based results.

To conclude, these results highlight the challenges and limitations of mimicking flow over sand waves with only roughness adjustments in flat seabed models. Although the method presented in this study does not determine a definitive form roughness value and is sensitive to the phase of the bathymetry, it offers a way to incorporate bedform-related information into the calibration process.

6 Recommendations for future research

Our findings and subsequent discussion led us to introduce a few recommendations for further investigation:

Firstly, due to time and storage limitations, our data collection focused on a single downwave location ($x = 20.75$ km from $y = 19$ to $y = 20.4$ km). Future studies should consider collecting data from multiple downstream locations to assess the impact of this choice on the calculated form roughness.

Moreover, to improve computational efficiency, our model employed an isotropic approach to represent increased effective roughness. This approach may underestimate the influence of rotation-induced form roughness. Future research should explore incorporating anisotropic roughness to get a better understanding of induced form roughness over a rotated sand wave field.

Additionally, while this study concentrated on a rotated sand wave field, further investigations are necessary to comprehend how various environmental settings, including water depth, tidal variations (e.g., multiple tidal constituents), and sand wave characteristics, affect the resulting form roughness values.

Finally, we observed a strong correlation between the phase-based criteria and the phase of the sand wave field bathymetry. This relationship might be linked to the coarsening of the grid resolution, resulting in a less smooth representation of the sand wave shapes compared to a finer grid. We recommend a dedicated 2DV study to determine if this dependency persists with a finer grid. Due to the significant computational cost of a finer 3D model, such an investigation in 3D is not advised at this stage.

References

Belderson, R. H., Johnson, M. A., & Kenyon, N. (1982). *Bedforms* (pp. 27–57). ISBN: 978-0-412-12970-4

Besio, G., Blondeaux, P., Brocchini, M., Hulscher, S. J. M. H., Idier, D., Knaapen, M. A. F., Németh, A. A., Roos, P. C., & Vittori, G. (2008). The morphodynamics of tidal sand waves: A model overview. *Coastal Engineering*, *55*(7), 657–670. https://doi.org/10.1016/j.coastaleng.2007.11.004

Besio, G., Blondeaux, P., Brocchini, M., & Vittori, G. (2004). On the modeling of sand wave migration. *Journal of Geophysical Research: Oceans*, *109*(C4). https://doi.org/10.1029/2002JC001622

Besio, G., Blondeaux, P., & Vittori, G. (2006). On the formation of sand waves and sand banks. *Journal of Fluid Mechanics*, *557*, 1–27. https://doi.org/10.1017/S0022112006009256

Borsje, B. W., de Vries, M. B., Bouma, T. J., Besio, G., Hulscher, S. J. M. H., & Herman, P. M. J. (2009). Modeling bio-geomorphological influences for offshore sandwaves. *Continental Shelf Research*, *29*(9), 1289–1301. https://doi.org/10.1016/j.csr.2009.02.008

Borsje, B. W., Kranenburg, W. M., Roos, P. C., Matthieu, J., & Hulscher, S. J. M. H. (2014). The role of suspended load transport in the occurrence of tidal sand waves. *Journal of Geophysical Research: Earth Surface*, *119*(4), 701–716. https://doi.org/10.1002/2013JF002828

Borsje, B. W., Roos, P. C., Kranenburg, W. M., & Hulscher, S. J. M. H. (2013). Modeling tidal sand wave formation in a numerical shallow water model: The role of turbulence formulation. *Continental Shelf Research*, *60*, 17–27. https://doi.org/10.1016/j.csr.2013.04.023

Brakenhoff, L., Schrijvershof, R., van der Werf, J., Grasmeijer, B., Ruessink, G., & van der Vegt, M. (2020). From Ripples to Large-Scale Sand Transport: The Effects of Bedform-Related Roughness on Hydrodynamics and Sediment Transport Patterns in Delft3D. *Journal of Marine Science and Engineering*, *8*(11), Article 11. https://doi.org/10.3390/jmse8110892

Campmans, G. H. P., Roos, P. C., de Vriend, H. J., & Hulscher, S. J. M. H. (2017). Modeling the influence of storms on sand wave formation: A linear stability approach. *Continental Shelf Research*, *137*, 103–116. https://doi.org/10.1016/j.csr.2017.02.002

Campmans, G. H. P., Roos, P. C., de Vriend, H. J., & Hulscher, S. J. M. H. (2018). The Influence of Storms on Sand Wave Evolution: A Nonlinear Idealized Modeling Approach. *Journal of Geophysical Research: Earth Surface*, *123*(9), 2070–2086. https://doi.org/10.1029/2018JF004616

Campmans, G. H. P., Roos, P. C., van der Sleen, N., & Hulscher, S. (2021). Modeling tidal sand wave recovery after dredging:effect of different types of dredging strategies. *Coastal Engineering*, *165*, 103862. https://doi.org/10.1016/j.coastaleng.2021.103862

Cheng, C. H., Soetaert, K., & Borsje, B. W. (2020). Sediment Characteristics over Asymmetrical Tidal Sand Waves in the Dutch North Sea. *Journal of Marine Science and Engineering*, *8*(6), Article 6. https://doi.org/10.3390/jmse8060409

Damen, J. M., van Dijk, T. A. G. P., & Hulscher, S. J. M. H. (2018). Spatially Varying Environmental Properties Controlling Observed Sand Wave Morphology. *Journal of Geophysical Research: Earth Surface*, *123*(2), 262–280. https://doi.org/10.1002/2017JF004322

Damveld, J. H., Borsje, B. W., Roos, P. C., & Hulscher, S. J. M. H. (2020). Horizontal and Vertical Sediment Sorting in Tidal Sand Waves: Modeling the Finite-Amplitude Stage. *Journal of Geophysical Research: Earth Surface*, *125*(10), e2019JF005430. https://doi.org/10.1029/2019JF005430

Deltares. (2023). *Delft3D-FLOW User Manual*. Deltares. https://content.oss.deltares.nl/delft3d4/Delft3D-FLOW_User_Manual.pdf

Deltares. (2024). *Delft3D Hydro-Morphodynamics User Manual*. Deltares. https://content.oss.deltares.nl/delft3d4/Delft3D-FLOW_User_Manual.pdf

Hulscher, S. J. M. H. (1996). Tidal-induced large-scale regular bed form patterns in a three-dimensional shallow water model. *Journal of Geophysical Research: Oceans*, *101*(C9), 20727–20744. https://doi.org/10.1029/96JC01662

Krabbendam, J., Nnafie, A., de Swart, H., Borsje, B. W., & Perk, L. (2021). Modelling the Past and Future Evolution of Tidal Sand Waves. *Journal of Marine Science and Engineering*, *9*(10), Article 10. https://doi.org/10.3390/jmse9101071

Lefebvre, A., & Winter, C. (2016). Predicting bed form roughness: The influence of lee side angle. *Geo-Marine Letters*, *36*(2), 121–133. https://doi.org/10.1007/s00367-016-0436-8

Lesser, G. R., Roelvink, J. A., van Kester, J. A. T. M., & Stelling, G. S. (2004). Development and validation of a three-dimensional morphological model. *Coastal Engineering*, *51*(8), 883–915. https://doi.org/10.1016/j.coastaleng.2004.07.014

McCave, I. N. (1971). Sand waves in the North Sea off the coast of Holland. *Marine Geology*, *10*(3), 199–225. https://doi.org/10.1016/0025-3227(71)90063-6

Morelissen, R., Hulscher, S. J. M. H., Knaapen, M. A. F., Németh, A. A., & Bijker, R. (2003). Mathematical modelling of sand wave migration and the interaction with pipelines. *Coastal Engineering*, *48*(3), 197–209. https://doi.org/10.1016/S0378-3839(03)00028-0

Nemeth, A., Hulscher, S. J. M. H., & de Vriend, H. J. (2003). Offshore sand wave dynamics, engineering problems and future solutions. *Pipeline and gas journal*, *230*(4), 67–69.

Portos-Amill, L., Roos, P. C., Damveld, J. H., & Hulscher, S. J. M. H. (2024). Modeling Form Roughness Induced by Tidal Sand Waves. *Journal of Geophysical Research: Earth Surface*, *129*(5), e2023JF007610. https://doi.org/10.1029/2023JF007610

Soulsby, R. (1997). *Dynamics of marine sands: A manual for practical applications*. Telford.

Styles, R., & Glenn, S. M. (2002). Modeling bottom roughness in the presence of wave-generated ripples. *Journal of Geophysical Research: Oceans*, *107*(C8), 24-1-24–15. https://doi.org/10.1029/2001JC000864

Tobias, C. J. (1989). Morphology of sandwaves in relation to current, sediment and wave data along the Eurogeul, North Sea. *Report GEOPRO*, *1*.

Torres, R., & Uncles, R. J. (2011). 2.17—Modeling of Estuarine and Coastal Waters. In E. Wolanski & D. McLusky (Eds.), *Treatise on Estuarine and Coastal Science* (pp. 395–427). Academic Press. https://doi.org/10.1016/B978-0-12-374711-2.00216-3

van der Meijden, R., Damveld, J. H., Ecclestone, D. W., van der Werf, J. J., & Roos, P. C. (2023). Shelf-wide analyses of sand wave migration using GIS: A case study on the Netherlands Continental Shelf. *Geomorphology*, *424*, 108559. https://doi.org/10.1016/j.geomorph.2022.108559

van Dijk, T. A. G. P., Best, J., & Baas, A. C. W. (2021). Subaqueous and Subaerial Depositional Bedforms. In D. Alderton & S. A. Elias (Eds.), *Encyclopedia of Geology (Second Edition)* (pp. 771–786). Academic Press. https://doi.org/10.1016/B978-0-08-102908-4.00187-9

van Dijk, T. A. G. P., & Kleinhans, M. G. (2005). Processes controlling the dynamics of compound sand waves in the North Sea, Netherlands. *Journal of Geophysical Research: Earth Surface*, *110*(F4). https://doi.org/10.1029/2004JF000173

van Gerwen, W., Borsje, B. W., Damveld, J. H., & Hulscher, S. J. M. H. (2018). Modelling the effect of suspended load transport and tidal asymmetry on the equilibrium tidal sand wave height. *Coastal Engineering*, *136*, 56–64. https://doi.org/10.1016/j.coastaleng.2018.01.006

van Rijn, L. C. (1993). *Principles of Sediment Transport in Rivers, Estuaries and Coastal Seas*. Aqua Publications. ISBN: 978-90-800356-2-1

van Rijn, L. C. (2007). Unified View of Sediment Transport by Currents and Waves. I: Initiation of Motion, Bed Roughness, and Bed-Load Transport. *Journal of Hydraulic Engineering*, *133*(6), 649–667. https://doi.org/10.1061/(ASCE)0733-9429(2007)133:6(649)

Wang, Z., Liang, B., Wu, G., & Borsje, B. W. (2019). Modeling the formation and migration of sand waves: The role of tidal forcing, sediment size and bed slope effects. *Continental Shelf Research*, *190*, 103986. https://doi.org/10.1016/j.csr.2019.103986

Wright, J., Colling, A., & Park, D. (1999). Chapter 2—Tides. In *Waves, Tides and Shallow-Water Processes* (Vol. 4, pp. 50–86). Butterworth-Heinemann. https://doi.org/10.1016/B978-008036372-1/50003-9

Zhou, J., Wu, Z., Zhao, D., Guan, W., Cao, Z., & Wang, M. (2022). Effect of topographic background on sand wave migration on the eastern Taiwan Banks. *Geomorphology*, *398*, 108030. https://doi.org/10.1016/j.geomorph.2021.108030

Zijl, F., Zijlker, T., Laan, S., & Groenenboom, J. (2022). *3D DCSM FM: a sixth-generation model for the NW European Shelf*. Deltares.

Appendix A: Effect of sand waves on tidal flow

We conduct an analysis to understand the impact of a sand wave field perpendicular to the dominant flow direction ($\psi_{sw} = 0°$) on tidal flow by examining the variations in the depth-averaged flow in the direction of tidal wave propagation (U) and the cross-tide flow component (V). We compare the case with a sand wave field to that of a flatbed, both forced by a propagating tidal wave and the Coriolis force at 52°N. We use the default sand wave field characteristics, with a wavelength of 100 m to have more sand waves over the domain (compared to using other wavelengths). In contrast, for the flatbed simulation, we considered only grain roughness (f_g).

The results for both the amplitude and phase of U and V are presented in Table 5 (note that the amplitude and phase are obtained based on the definition and procedure mentioned in subsection 2.2). The results show that the presence of sand waves lead to a decrease in amplitude and a phase shift in U. In V, however, the sand wave field does not influence the amplitude of the depth-averaged flow but leads to a phase shift only.

These results are illustrated in Figure 26 and Figure 27 for U and V, respectively. In Figure 26 it can be observed the difference between a sand wave and flatbed simulation, highlighting the differences in the amplitude of U. Similarly, Figure 27b indicates that the maximum V for a flatbed (dashed purple line) is slightly higher than the maximum for a sand wave field (solid yellow line). However, the minimum V for a sand wave field is more negative than the one for a flatbed, resulting in both having the same amplitude.

Table 5 Depth-averaged flow both along-tide and cross-tide for a flatbed and sand wave field simulation.

	Depth-averaged flow in the direction of the tidal wave propagation U		**Depth-averaged flow in cross-tide direction V**	
	Amplitude (m/s)	**Phase (rad)**	**Amplitude (m/s)**	**Phase (rad)**
Sand wave field	0.5805	0.3062	0.0266	-3.0071
Flatbed	0.5813	0.2988	0.0266	-3.0084

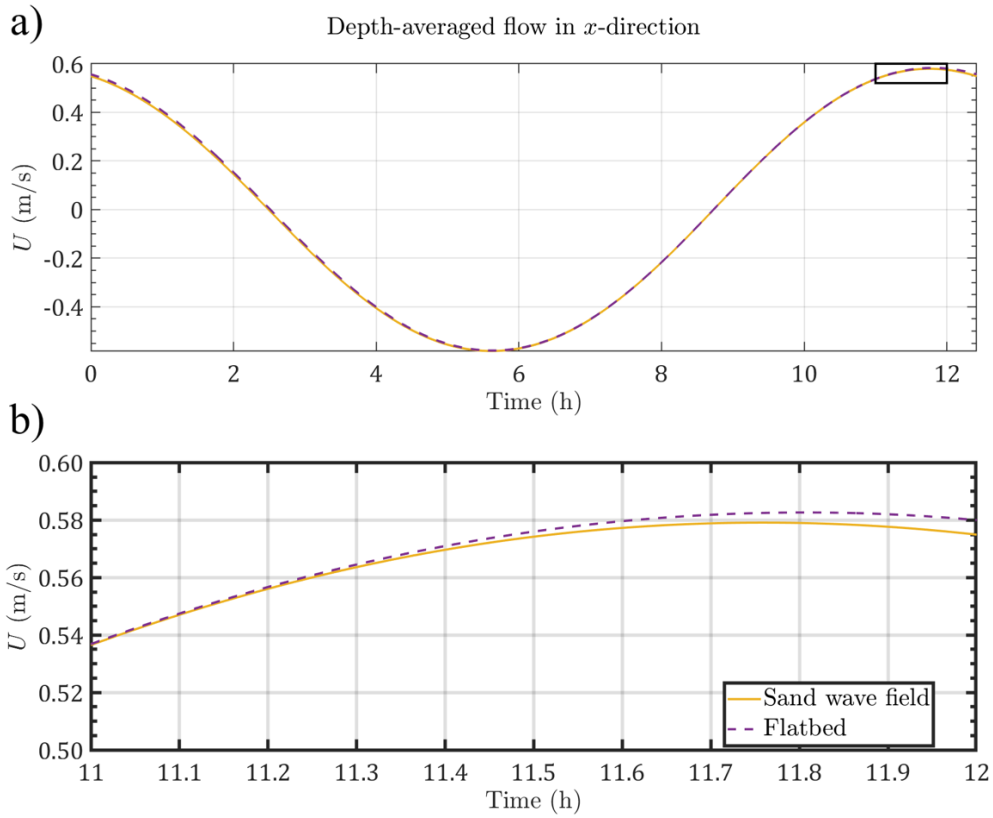

Figure 26 (a) Depth-averaged flow in the direction of the tidal wave propagation comparing the situation with a flatbed (dashed purple line) and a sand wave field (solid yellow line) simulation. The black box indicates the zoomed-in region in (b).

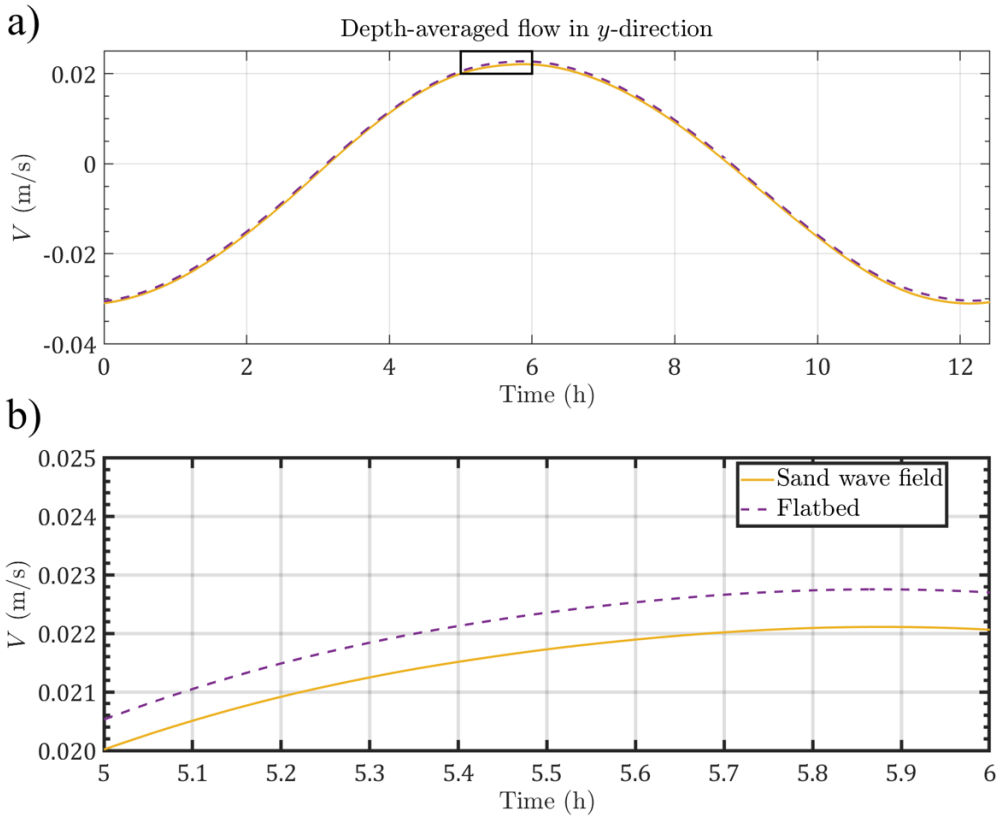

Figure 27 (a) Depth-averaged flow in cross-tide direction comparing the situation with a flatbed (dashed purple line) and a sand wave field (solid yellow line) simulation. The black box indicates the zoomed-in region in (b).

Appendix B: Coriolis force effect in the model

Tides are influenced by the Coriolis force, yielding a counterclockwise rotation in the Northern Hemisphere (Wright et al., 1999). The impact of the Coriolis force on tidal flow is analyzed by comparing 3D models with and without it, as well as with the 2DV model (with the same time step Δt and minimum grid spacing Δx_{min}) to discern differences. The simulations are carried out over a sand wave field with the default characteristics (see Section 2.4). Due to the Coriolis force, there is a relatively small flow in the y-direction (see Figure 28 and Figure 29a). Moreover, as expected, there is negligible flow in the y-direction when the Coriolis force is not incorporated into the model (see Figure 28 and Figure 29b).

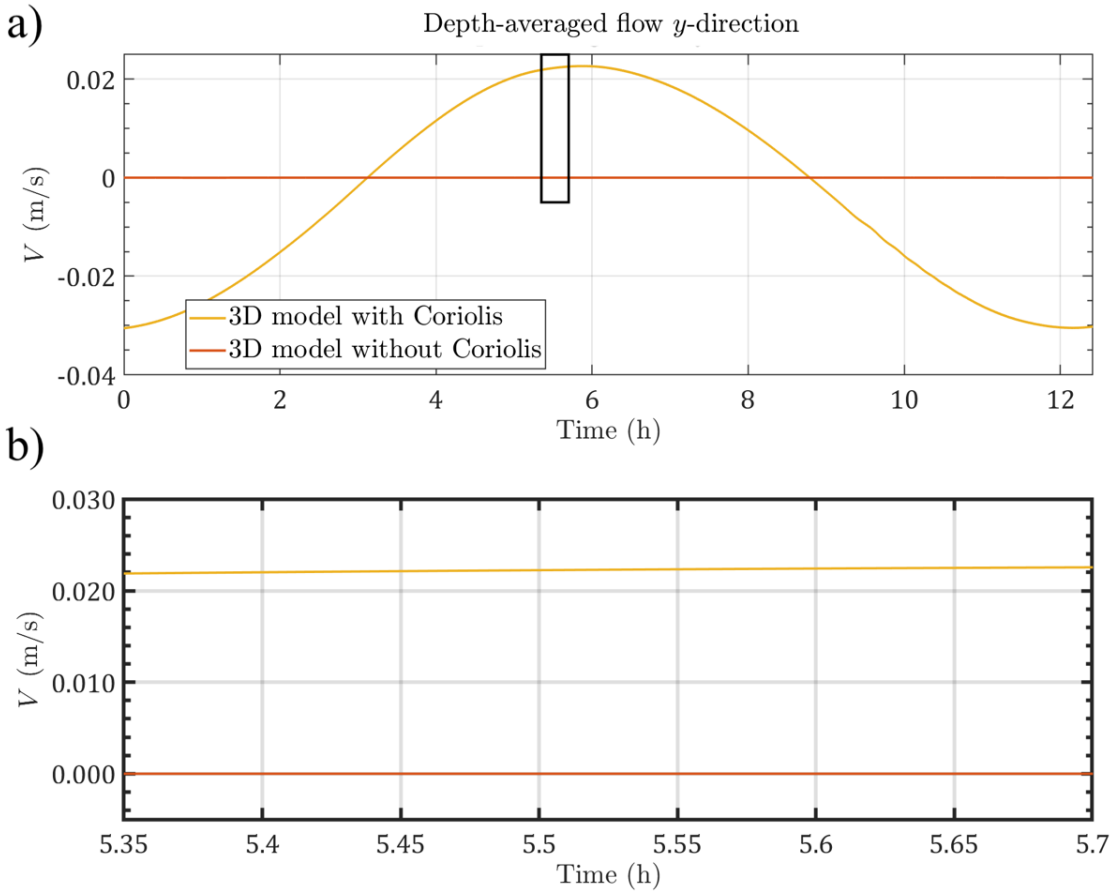

Figure 28 (a) Depth-averaged flow in the cross-tide direction over the default sand wave with and without the Coriolis force. The black box indicates the zoomed-in region in (b).

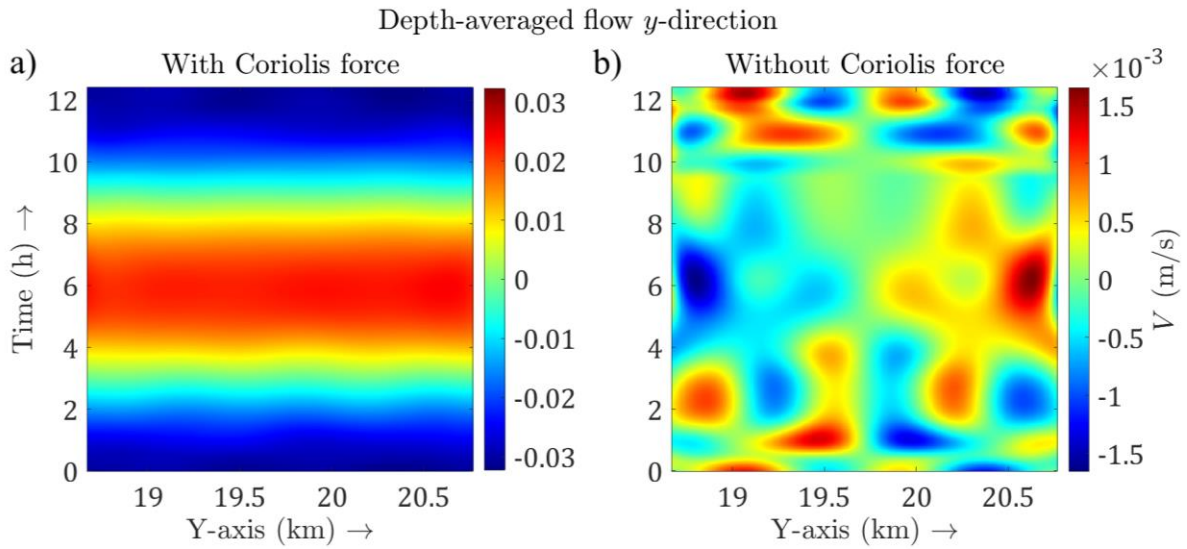

Figure 29 Depth-averaged flow in the cross-tide direction along the y-axis: a) Model including Coriolis force. b) Model without Coriolis force. Note the different scale of the color bars.

The results in terms of the depth-averaged flow in the direction of the tidal wave propagation (U) and sea surface elevation (ζ) values are presented in Table 6. U and ζ over a tidal signal for the 3D models with and without the Coriolis force, as well as the 2DV model, are illustrated in Figure 30 and Figure 31, respectively. As expected, these results show that ζ in a 3D model without Coriolis properly matches the 2DV model. In contrast, the 3D model with Coriolis exhibits a lower amplitude and a phase shift. Interestingly, all models display discrepancies in both amplitude and phase for U. We initially expected the 3D model without Coriolis and the 2DV model to show similar values for these parameters. This discrepancy likely arises from the open boundary conditions at $y = 0, L_y$ applied in the 3D model. These boundary conditions are not imposed in the 2DV model. Furthermore, the Coriolis force in the 3D model leads to a higher U, a lower ζ, and the emergence of flow in cross-tide direction (V). These findings highlight the significant differences in how sand wave fields influence tidal flow between 2DV and 3D models, particularly models including the Coriolis force.

Table 6 Depth-averaged flow in the direction of the tidal wave propagation and sea surface elevation downwave of the sand wave field for the 3D models with and without Coriolis force and the 2DV model.

	Depth-averaged flow in the direction of the tidal wave propagation U		**Sea surface elevation ζ**	
	Amplitude (m/s)	**Phase (rad)**	**Amplitude (m)**	**Phase (rad)**
3D model with Coriolis	0.5841	0.3032	1.0669	0.2866
3D model without Coriolis	0.5831	0.3040	1.0718	0.2888
2DV model	0.5855	0.2994	1.0717	0.2888

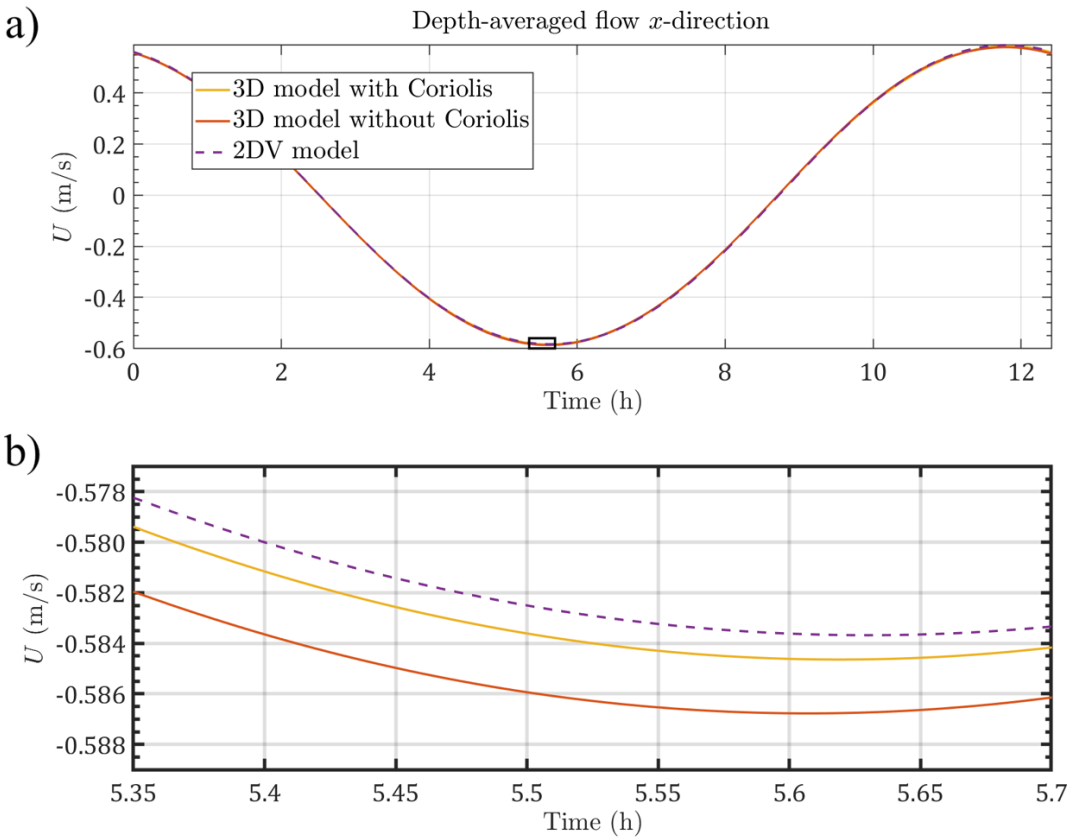

Figure 30 (a) Depth-averaged in the direction of the tidal wave propagation downwave of the sand wave field for the 3D models with and without Coriolis force and the 2DV model. The black box indicates the zoomed-in region in (b).

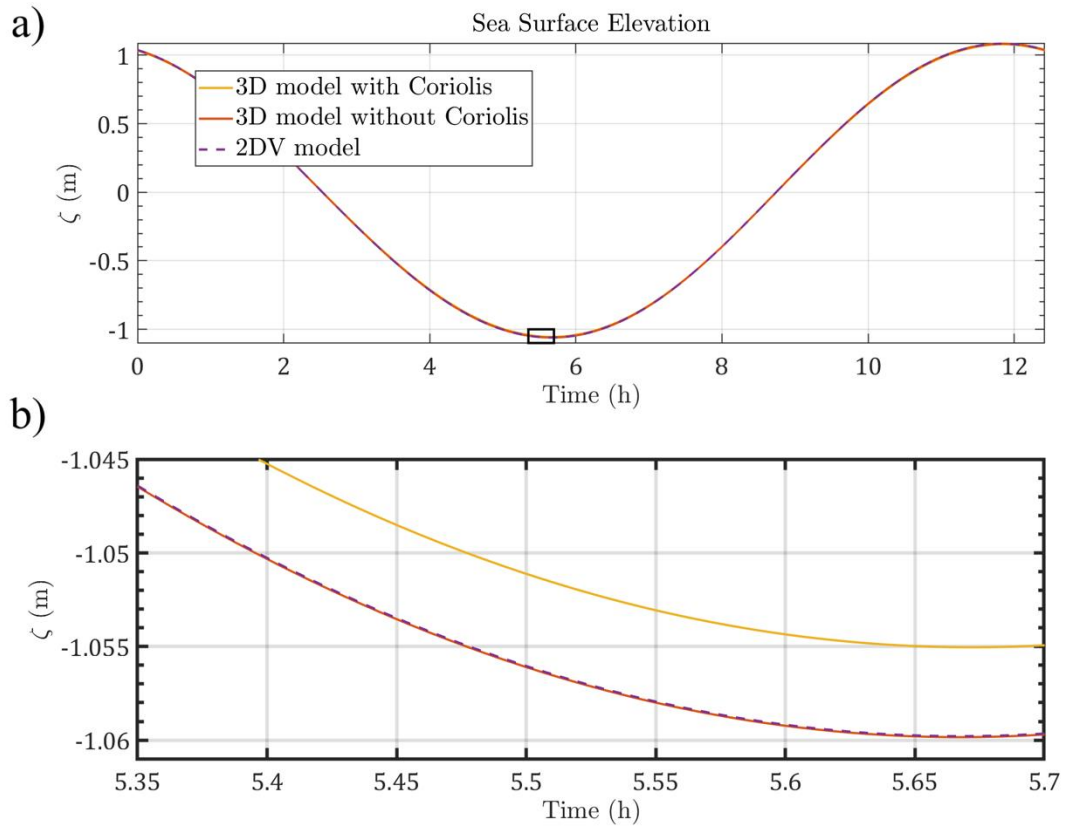

Figure 31 (a) Sea surface elevation downwave of the sand wave field for the 3D models with and without Coriolis force and the 2DV model. The black box indicates the zoomed-in region in (b).

Appendix C: Effect of different mean water depth in rotated sand wave fields

This section explores the influence of mean water depth variation on form roughness calculations in the presence of rotated sand wave fields. Sand wave fields oriented at specific angles can cause slight discrepancies in mean water depth within the sand wave area ($Area_{sw}$) and the overall model domain. To isolate the effect of this depth change on our results, we analyze simulations with a flatbed with a different mean water depth. We choose to analyze the sand wave field rotated 75 degrees, as it exhibits the most significant deviation in mean water depth within the central area ($H = 29.981$ m) compared to the original mean water depth ($H = 30$ m). In the flatbed case, we replicate the mean water depth of the rotated sand wave field ($H = 29.9983$ m, in the central area) while maintaining a constant water depth of 30 meters elsewhere in the model domain. This configuration ensures the same mean water depth ($H = 29.987$ m) across the entire model domain for both the rotated sand wave field and the flatbed.

We then calculate the corresponding form roughness (refer to subsection 2.5) for a flatbed with different mean water depths to match the depth-averaged flow in the direction of the tidal wave propagation U and sea surface elevation ζ of the rotated sand wave field. Table 7 summarizes the resulting form roughness coefficients for the different criteria. The results indicate that the minimal change in mean water depth has a negligible impact on the form roughness coefficient. Consequently, for various rotation angles, the slight variations in mean water depth associated with rotated sand wave fields can be considered negligible as they do not significantly affect the resulting form roughness.

Table 7 Corresponding form roughness coefficients over a flatbed with different mean water depth to match the depth-averaged flow in the direction of the tidal wave propagation and sea surface elevation either amplitude or phase-based over a rotated sand wave field ($\psi_{sw} = 75°$).

Flatbed simulation with different H	**Depth-averaged flow in the direction of the tidal wave propagation U**		**Sea surface elevation ζ**	
H (m)	**Amplitude**	**Phase**	**Amplitude**	**Phase**
30	0	0.0016	0.0002	0.0031
29.987	0	0.0016	0.0002	0.0031